



Extrasolar planets detections and statistics through gravitational microlensing

Arnaud Cassan

► To cite this version:

Arnaud Cassan. Extrasolar planets detections and statistics through gravitational microlensing. Astrophysics [astro-ph]. Université Pierre et Marie Curie, 2014. <tel-01088218>

HAL Id: tel-01088218

<https://hal.science/tel-01088218v1>

Submitted on 2 Jan 2015

HAL is a multi-disciplinary open access archive for the deposit and dissemination of scientific research documents, whether they are published or not. The documents may come from teaching and research institutions in France or abroad, or from public or private research centers.

L'archive ouverte pluridisciplinaire **HAL**, est destinée au dépôt et à la diffusion de documents scientifiques de niveau recherche, publiés ou non, émanant des établissements d'enseignement et de recherche français ou étrangers, des laboratoires publics ou privés.



HAL Authorization

Université Pierre et Marie Curie

Mémoire d'Habilitation à Diriger des Recherches

**Extrasolar planets detections and statistics
through gravitational microlensing**

par

Arnaud Cassan

*Institut d'Astrophysique de Paris (UMR7095 UPMC/CNRS)
98bis boulevard Arago, 75014 Paris, France.*

Présentée et soutenue publiquement le

1 octobre 2014

devant le jury composé de :

M. Vincent Coudé du Foresto	Président
M. Marc Ollivier	Rapporteur
M. Tristant Guillot	Rapporteur
M. Shude Mao	Rapporteur
M. Joachim Wambsganss	Examineur
M. Keith Horne	Examineur

Extrasolar planets detections and statistics through gravitational microlensing

Arnaud Cassan

Université Pierre et Marie Curie, Institut d'Astrophysique de Paris,
UMR7095 CNRS-UPMC, 98bis boulevard Arago, 75014 Paris, France

Abstract: Gravitational microlensing was proposed thirty years ago as a promising method to probe the existence and properties of compact objects in the Galaxy and its surroundings. The particularity and strength of the technique is based on the fact that the detection does not rely on the detection of the photon emission of the object itself, but on the way its mass affects the path of light of a background, almost aligned source. Detections thus include not only bright, but also dark objects. Today, the many successes of gravitational microlensing have largely exceeded the original promises. Microlensing contributed important results and breakthroughs in several astrophysical fields as it was used as a powerful tool to probe the Galactic structure (proper motions, extinction maps), to search for dark and compact massive objects in the halo and disk of the Milky Way, to probe the atmospheres of bulge red giant stars, to search for low-mass stars and brown dwarfs and to hunt for extrasolar planets. As an extrasolar planet detection method, microlensing nowadays stands in the top five of the successful observational techniques. Compared to other (complementary) detection methods, microlensing provides unique information on the population of exoplanets, because it allows the detection of very low-mass planets (down to the mass of the Earth) at large orbital distances from their star (0.5 to 10 AU). It is also the only technique that allows the discovery of planets at distances from Earth greater than a few kiloparsecs, up to the bulge of the Galaxy. Microlensing discoveries include the first ever detection of a cool super-Earth around an M-dwarf star, the detection of several cool Neptunes, Jupiters and super-Jupiters, as well as multi-planetary systems and brown dwarfs. So far, the least massive planet detected by microlensing has only three times the mass of the Earth and orbits a very low mass star at the edge of the brown dwarf regime. Several free-floating planetary-mass objects, including free-floating planets of about Jupiter's mass, were also detected through microlensing. Detections and non-detections inform us on the abundance of planets as a function of planetary mass and orbital distance. Recent microlensing studies imply that low-mass planets, in particular super-Earths, are far more abundant than giant planets, and reveal that there are, on average, one or more bound planets per Milky Way star. Future microlensing surveys will dramatically increase the number of microlensing alerts, thus providing unprecedented constraints on the planetary mass function, down to the mass of the Earth.

Mémoire d'Habilitation à Diriger des Recherches, January 2014.

Note to the reader: Although the original purpose of this document was to present the contributions of the author in the topics covered in this Mémoire, it has been written primarily as a review.

Contents

I. Introduction	3
II. Gravitational microlensing as an astrophysical tool	4
A. Microlensing events	4
1. The lens equation	4
2. Source magnification	7
3. Critical curves and caustics	10
4. Light curve anomalies	14
B. Events follow-up strategy	17
1. The "alert an follow-up" observing strategy	17
2. Two detection channels	20
3. Real-time data reduction and modeling	20
4. Further observations	21
C. Astrophysical applications	22
1. Probing the stellar atmospheres of Galactic bulge giants	22
2. Mass and distance of isolated and binary stars	27
3. Detection of brown dwarfs	29
III. Detection and statistics of extrasolar planets	32
A. 2003-2005: microlensing milestone discoveries	33
1. The first exoplanet detected through microlensing	33
2. First cool super-Earth: OGLE 2005-BLG-390Lb	34
B. Microlensing planet discoveries	36
1. A panorama of detections	36
2. Cool super-Earths and Neptune-like planets	37
3. Massive planets around late-type stars	38
4. Free-floating planets	39
C. Statistical studies of Galactic populations of extrasolar planets	40
1. 1995-2000: first upper limits on exoplanet frequency	40
2. The 2005-08 high-magnification sample	41
3. PLANET+OGLE 2002-07: One or more planets per Milky Way star	42
IV. Towards a large scale microlensing planet search	45
A. A new generation of ground-based telescopes	45
1. Networks of robotic telescopes with wide-field cameras	45
2. Astrometry and interferometry	46
B. Microlensing planet search from space	47
1. Advantages	47
2. Planet yield estimation	48
C. Advanced modeling	50
1. Numerical methods	50
2. Light curve features-based modeling	51
3. Bayesian analysis of microlensing events	54
4. Towards automated modeling softwares	54
V. Summary and prospects	56

I. Introduction

For centuries, the night sky has been observed by eye. The interpretation of what could be seen long relied on the skills and imagination of astronomers and philosophers, leading to theories of unequal success. With Galileo and the use of the first telescopes, more details were found about the structures and distances of astronomical objects, but still a large fraction of the sky was unseen, because only a narrow fraction of the electromagnetic spectrum was accessible to the naked eye. The discovery of spectroscopy by Fraunhofer in the 19th century and its steady development in astronomy revealed a much more crowded sky: emitting, reflecting, absorbing matter became subjects of quantitative studies. But relatively far, faint, compact objects were still out of reach of any observational technique.

At the turn of the 20th century, General Relativity would fortunately provide a new and original technique to see the invisible. In a famous article published in 1936, Einstein derived the equations of the bending of light rays originating from a background star when passing in the vicinity of a foreground star, what is called today “gravitational microlensing”. For the first time, the idea was raised that a star could be detected by the gravitational influence it had on the path of light coming from another star. At the time the article came out, however, observational facilities were not developed enough yet to seriously envisage detecting a microlensing effect. Einstein himself concluded: “there is no great chance of observing this phenomenon”.

Indeed, for many years stellar microlensing was mostly ignored. But sooner or later, visionary ideas always come back: about 50 years after Einstein’s publication, the astrophysicist Bohdan Paczyński revisited the basic ideas of microlensing observations, in a seminal article published in 1986. The original idea of the paper was to propose a new method to detect hypothetic dark, compact, massive halo objects (MACHOs) as a possible form of dark matter in the Milky Way. Paczyński’s work provided new quantitative arguments on microlensing events occurrence rate with much more optimistic observational perspectives, and ended his argumentation with ideas on how to put the method into practice. In this special context, a great attention was rapidly paid to microlensing as a potential technique to solve the missing dark matter problem. A number of observational searches with line of sights towards the Large and Small Magellanic Clouds and the Galactic center in particular were subsequently initiated beginning of the 1990s: MACHO (Massive Compact Halo Object), EROS (Experience pour la Recherche d’Objets Sombres) and OGLE (Optical Gravitational Lensing Experiment). In 1993, the first stellar microlensing events were detected independently by the MACHO and EROS collaborations. These detections mark the birth of microlensing as an observational technique. In 2014, about 3000 events are detected every year, which provide unique astrophysical informations in several fields of research in astronomy and astrophysics.

After his 1986’s paper, Paczyński investigated further the possible implications of microlensing as an observational method. With Shude Mao, he published in 1991 a second seminal paper, in which the two authors claimed that a massive microlensing search towards the Galactic bulge could lead to the discovery of the

first extrasolar planetary systems. Nevertheless, this apparent optimism had to be tempered by the fact that the same year, Paczyński used the expression “science fiction” (quoted by S. Mao) when commenting the article in a conference. As a matter of fact, the first exoplanet in orbit around a main sequence star was detected in 1995 by radial velocimetry, and it took a full decade of improvements in the strategy and the instruments before the first microlensing planet was detected in 2003.

After the microlensing pioneer times of decade 1993-2003, planets started to be detected at an increasing rate. Compared to concurrent planet detection methods, microlensing detections bring unique information on planetary populations that justified the strong and steady efforts deployed to make the technique work. While most planets detected with other methods are detected close to their stars, prime targets of microlensing are planets located beyond the snow line of their stars, where ices can start to form. A full understanding of the demographics of extrasolar planet in the Galaxy thus relies on the combination of the different observational techniques. During decade 2003-13, the most important microlensing results include the discovery of the first ever cool super-Earth planet (2005), the discovery of Jupiter-mass free-floating planets (2012), and first constraints on the planetary mass function for a wide range of masses and orbital distances (2012). At the end of a decade filled with discoveries, microlensing observations find that, on average, every Milky Way star has a planet, and that planets around stars are the rule rather than the exception.

The manuscript is organized as follows. In section II, we introduce the microlensing technique, and present astrophysical applications and results. Most specifically, we devote full section III to planetary microlensing, where planet discoveries and statistical results are discussed in the larger context of planet formation and evolution. In section IV, we address current and future developments of microlensing, both on an observational and modeling point of view. We conclude on prospects of microlensing observations to exoplanetary sciences.

II. Gravitational microlensing as an astrophysical tool

A. *Microlensing events*

1. The lens equation

Gravitational microlensing describes the bending of light from background source stars due to the gravitational field of compact objects crossing the observer-source line-of-sight, and acting as lenses. In general, multiple images of the source are produced. Let us consider a distant background *source* star, that is located at angular position β from the line-of-sight of a closely aligned point-like foreground *lens* star (Fig. 1). Light rays passing in the vicinity of the lens will be bent by gravity by an angle $\hat{\alpha} \ll 2\pi$ given by

$$\hat{\alpha} = \frac{4GM}{c^2} \frac{1}{|b|}, \quad (1)$$

where $|b|$ is the closest approach distance of the light ray from the lens, M is the total mass of the lens, c the speed of light and G the gravitational constant.

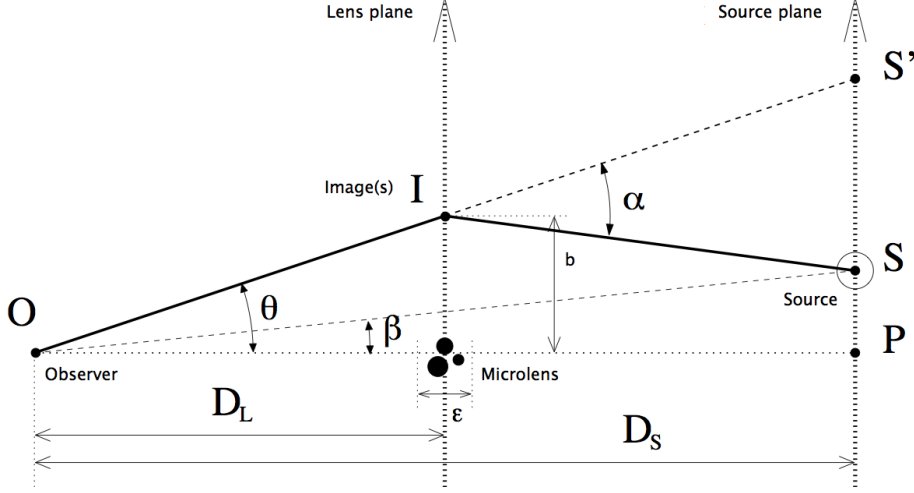


Figure 1: Geometry of a microlensing event. The source is located in the background, and is lensed by a foreground lensing star or planetary system (figure adapted from Cassan 2005).

Let D_L and D_S be the observer-lens and observer-source distances. From simple geometry and considering that all angles are very small, it follows that $(D_S - D_L) \hat{\alpha} \simeq D_S (\theta - \beta)$, where θ is the angle between the observer-lens line-of-sight and the direction of the light ray bent towards the observer. From an observer's point of view, the image of the source appears to be at angular position θ rather than β . We now introduce two-dimensional angles, to account for the fact that a light ray is always bent towards the lens¹, and replace $1/b$ by $b/|b|^2$ in Eq. (1). Then, one has $b \simeq D_L \theta$, which leads to the *lens equation* (without gravitational shear) that geometrically relates β and θ :

$$\beta = \theta - \frac{D_S - D_L}{D_S} \hat{\alpha} = \theta - \frac{4GM}{c^2} \frac{D_S - D_L}{D_S D_L} \frac{\theta}{|\theta|^2}. \quad (2)$$

For a given angular position β of a point source, the position θ of a given point-like image can be computed from the lens equation. In the case of a multiple lens, each component of the lens exerts a gravitational pull on the light rays, so that the resulting angular deviation is the linear sum of the individual deviations (assuming a thin gravitational lens). The lens equation for N point-mass lenses then reads

$$\beta = \theta - \frac{D_S - D_L}{D_S} \sum_{i=1}^N \hat{\alpha}_i = \theta - \frac{4GM}{c^2} \frac{D_S - D_L}{D_S D_L} \sum_{i=1}^N q_i \frac{\theta - \theta_i}{|\theta - \theta_i|^2}, \quad (3)$$

where θ_i are the angular positions of the lens components, of mass ratio q_i relative to the total mass of the lens. The form of equations Eq. (2) or (3) allows to

¹This means that the angles considered here have two components projected in the plane of the sky, e.g. $\beta = (\beta_x, \beta_y)$, to account for possible multiple and non-aligned images (Bourassa & Kantowski 1975).

introduce a typical microlensing angle θ_E , called *angular Einstein radius*:

$$\theta_E \equiv \sqrt{\frac{4GM}{c^2} \left(\frac{D_S - D_L}{D_S D_L} \right)}. \quad (4)$$

In the ideal case of a single point-mass lens perfectly aligned with a point-source, one has $\beta = 0$ and according to Eq. (2), the lens equation reduces to $\theta = \theta_E$. This means that the image of the source is a circle of angular radius θ_E , or *Einstein ring*, instead of a set of discrete point-like images. It is convenient to introduce π_{rel} , the *relative lens-source parallax*, as:

$$\pi_{\text{rel}} \equiv \frac{\text{AU}}{D_L} - \frac{\text{AU}}{D_S} = \text{AU} \left(\frac{D_S - D_L}{D_S D_L} \right), \quad (5)$$

and the corresponding vector which direction is the lens-source relative motion. Eq. (4) can now be simply written

$$\theta_E = (\kappa M \pi_{\text{rel}})^{1/2}, \quad (6)$$

with $\kappa \simeq 4G/c^2 \text{AU} \simeq 8.144 \text{mas}/M_\odot$, and where M is expressed in solar masses (M_\odot) and π_{rel} in mas. In practice, if D_L and D_S are expressed in kpc, one gets immediately the numerical value of π_{rel} in mas. In Galactic microlensing, most microlens stars are red dwarfs, with typical masses $\sim 0.5 M_\odot$ and typical $\pi_{\text{rel}} \sim 0.1 \text{mas}$. Hence, numerical values of the angular Einstein radius can be conveniently computed from

$$\theta_E \simeq 0.638 \left(\frac{M}{0.5 M_\odot} \right)^{1/2} \left(\frac{\pi_{\text{rel}}}{0.1 \text{mas}} \right)^{1/2} \text{mas}. \quad (7)$$

With typical values of θ_E of order of a fraction of a mas, it is impossible with classical telescopes to resolve the individual images of the source (contrary to strong lensing effects that create giant gravitational arcs of distant galaxies or quasars). Such lenses are thus called *microlenses*, and *microlensing events* are discovered by a *flux magnification effect* as shown later.

The plane of the sky located at the lens distance D_L is called the *lens plane*, while at the source distance D_S it is called the *source plane*. Most source stars reside within the Galactic bulge ($D_S \sim 8 \text{kpc}$), while microlenses can be anywhere between the source and observer. The *linear radius* of the Einstein ring (also called *Einstein radius*) at the lens distance D_L reads

$$R_E \equiv D_L \theta_E \simeq 2.85 \left(\frac{M}{0.5 M_\odot} \right)^{1/2} \left(\frac{x(1-x)}{0.25} \right)^{1/2} \left(\frac{D_S}{8 \text{kpc}} \right)^{1/2} \text{AU}, \quad (8)$$

where $x = D_L/D_S$. The maximum value of R_E is obtained for $x = 0.5$, *i.e.* for a lens at mid-distance from the observer and source. For a typical microlensing event, the Einstein radius ranges from 0.2 to 20 AU, which are typical sizes of planetary orbits. Planets around the lens with orbital separations in this range at the date of the observation will therefore have a good chance to be detected.

With Eq. (3) normalized by θ_E , complex numbers can be used to express the lens equation. Let us define $\zeta = \xi + i\eta = \beta/\theta_E$ as the position of a point-source in the source plane, $z = x + iy = \theta/\theta_E$ the position of an individual point-like image in the lens plane, and $z_i = \theta_i/\theta_E$ the position of the i^{th} mass component of the lens onto the lens plane. The lens equation now reads:

$$\zeta = z - \sum_{i=1}^N \frac{q_i}{\bar{z} - \bar{z}_i}, \quad (9)$$

where $\bar{z} = |z|^2/z$ denotes the complex conjugate of z . For a given position ζ of the point-source S , there exists a finite number of solutions $z^{(k)}$ for z , which are the source images I_k . To solve the lens equation in complex notations, a classical method (Witt 1990) consists in transforming Eq. (9) into a complex polynomial in z of degree $N^2 + 1$. Not all solutions of the polynomial, however, are solutions of Eq. (9): there exists a maximum of $5(N - 1)$ images (Rhie 2003), the exact number depending on the position of the source relative to the lens.

2. Source magnification

The lens produces several images of the source star, that are too close to each others (a fraction of a mas) to be resolved individually by a classical telescope². If an extended source with a uniform brightness profile is lensed, the resulting images of the source star will be distorted. An important property of gravitational lensing is that the *surface brightness* is conserved (same as for a magnifying glass that increases the bulk size of an object but not its brightness), so that the ratio μ of the total flux of the images to that of the source is simply the ratio of the total surface of the images to that of the source,

$$\mu = \frac{1}{\mathcal{A}_S} \sum_k \mathcal{A}_{I_k}. \quad (10)$$

In general, the sum of the area of the images is greater than the area of the source, so that the net lensing effect is an apparent *magnification* (or *amplification*) of the source flux. μ is therefore called the *magnification factor* (or simply *magnification*).

Let us now consider an infinitesimal extended source at position $\zeta = (\xi, \eta)$ and of area $d\Sigma_S = d\xi d\eta$, that is mapped into an image k at position $z_k = (x_k, y_k)$ with area $d\Sigma_I = dx dy$. The ratio of the two areas reads

$$\mu_k = \frac{d\Sigma_I}{d\Sigma_S} = \frac{dx dy}{d\xi d\eta} = \frac{1}{|J|}, \quad (11)$$

where J is the determinant of the Jacobian matrix of the mapping $z \rightarrow \zeta$,

$$J = \left| \frac{\partial(\eta, \xi)}{\partial(x, y)} \right|_{z_k}, \quad (12)$$

²Interferometers would however distinguish the different individual images.

evaluated at the image position z_k . Using complex numbers, and considering z and \bar{z} as two independent variables, Witt (1990) demonstrated that in general the determinant of the Jacobian can be written as

$$J = \left(\frac{\partial \zeta}{\partial z} \right)^2 - \frac{\partial \zeta}{\partial \bar{z}} \frac{\partial \bar{\zeta}}{\partial \bar{z}}, \quad (13)$$

or, using Eq. (9),

$$J = 1 - \left| \sum_{i=1}^N \frac{q_i}{(\bar{z} - \bar{z}_i)^2} \right|^2. \quad (14)$$

The Jacobian can be either positive or negative, and has respective *positive* or *negative parity*. According to Eq. (11), the absolute value of the inverse of the Jacobian is the *point-source magnification* of the individual image k , or $\mu_k = |J^{-1}(z_k)|$. The *total point-source magnification* is then given by

$$\mu(\zeta) \equiv \sum_k \mu_k = \sum_k \left| \frac{1}{J(z_k)} \right|. \quad (15)$$

For an extended source with arbitrary intensity profile \mathcal{I} , the *finite-source magnification* is given by integrating the point-source magnification over the source surface,

$$\mu = \frac{1}{\iint_{\mathcal{A}_S} \mathcal{I} d\xi d\eta} \sum_k \iint_{\mathcal{A}_S} \mu_k \mathcal{I} d\xi d\eta, \quad (16)$$

where \mathcal{I} is directly mapped from ζ to z_k since surface brightness is conserved. In the latter formula, integration is performed over the source star, and as long as J does not vanish, it is a convenient way to compute the magnification. When $J = 0$, this integration scheme is not appropriate and it may be preferable to integrate over the images:

$$\mu = \frac{1}{\iint_{\mathcal{A}_S} \mathcal{I} d\xi d\eta} \sum_k \iint_{\mathcal{A}_{I_k}} \mathcal{I} dx dy. \quad (17)$$

Although there is no more singularity in the integrand, the images shapes (integration contours) have to be determined, which poses other challenges. Mathematical and numerical methods to compute the magnification are discussed later.

Single lenses

Single lenses (isolated stars) are the simplest microlensing systems (Fig. 2) but describe most observed microlensing light curves. The single lens equation reduces to

$$\zeta = z - \frac{1}{\bar{z}}, \quad (18)$$

where the lens is chosen to be at the origin of the coordinates system. As illustrated in Fig. 2, two distorted images (blue disks) of an extend source (blue circle) are produced by a single point lens (black dot). Since the argument ϕ of z

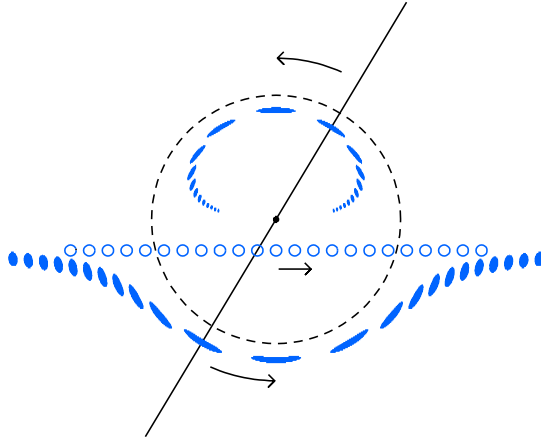


Figure 2: A single point-lens (isolated star, black dot) produces two images (blue disks) of an extended source star (blue circle). The lens, source and images are always aligned (black solid line), with the minor image within the Einstein ring (dashed circle) and the major image outside. The arrows indicate how the images move when the source follows a rectilinear motion relative to the lens and observer (figure adapted from Paczynski 1996).

is the same as that of ζ , the argument of $1/\bar{z}$ must also be ϕ , and the two images must be aligned with the source and the lens (black solid line in the figure). The images are found by solving $u = r - 1/r$, where $\zeta = ue^{i\phi}$ and $z = re^{i\phi}$, which gives the two solutions r_+ and r_- along the black line

$$r_{\pm} = \frac{u \pm \sqrt{u^2 + 4}}{2}. \quad (19)$$

The image inside the Einstein ring (dashed circle) is of negative parity and is called the *minor image*, while the image outside has positive parity and is called the *major image*. If the lens had a companion located near one of these images, its gravitational field would distort further the shape of the images and produce a detectable magnification anomaly. This is the basic principle of planet detection *via* microlensing. The magnification of the minor and major images can be computed from Eq. (14), leading to $\mu_{\pm} = 1/(1 - |z_{\pm}|^4) = 1/(1 - r_{\pm}^4)$, or using Eq. (19)

$$\mu_{\pm} = \pm \frac{\left(u \pm \sqrt{u^2 + 4}\right)^2}{4u\sqrt{u^2 + 4}}. \quad (20)$$

The total magnification is then

$$\mu = \mu_- + \mu_+ = \frac{u^2 + 2}{u\sqrt{u^2 + 4}}. \quad (21)$$

Single-lens magnification curves have a typical bell-shape aspect, as illustrated in Fig. 3 for different source trajectories.

Let us assume an extended circular source of radius ρ in θ_E units. When the source approaches the lens closer than around $u_0 \leq 3\rho$, finite source can be detected. Using an adequate parametrization to integrate over the two images contours according to Eq. (17), Witt & Mao (1994) found a semi-analytical formula of the magnification of a circular source by a single lens, involving three elliptic integrals. The magnification of a circular uniform source can then be computed very efficiently, to the desired numerical precision. For a limb-darkened

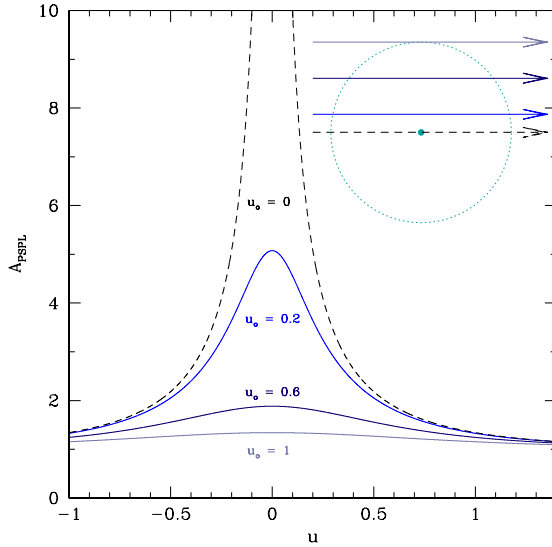


Figure 3: Typical single-lens magnification curves (bell-shaped curves), for rectilinear source trajectories of different impact parameters. The peak magnification is obtained when the source is at the closest distance from the lens u_0 (in θ_E units), and behaves as $1/u_0$ when $u_0 \rightarrow 0$ (figure from Cassan 2005).

source, this formula can be applied to discrete rings of uniform brightness, however, it is more efficient to use the approximate formula found by Gould (1994) and Yoo et al. (2004) when possible:

$$\mu_{\text{ext}} \simeq \mu(u) B_0(z), \quad (22)$$

where $z = u/\rho$ and

$$B_0(z) = \frac{4}{\pi} z E \left(\arcsin \min \left(1, \frac{1}{z} \right), z \right), \quad (23)$$

and where E is the incomplete elliptic integral of the second kind. This formula holds for small impact parameters ($u_0 \ll 1$), where the point-source magnification behaves as $\mu(u) \simeq u^{-1}$. It is interesting to note that parameters u and z are arguments of two independent functions. One-dimensional discretization of the semi-analytical integral is thus possible and allows very efficient calculation. Yoo et al. (2004) further derived expressions of functions, B_1 and $B_{1/2}$ for linear and square-root limb-darkening laws respectively.

3. Critical curves and caustics

Curves in the lens plane for which $J = 0$ (infinite point-source magnification) are called *critical lines*. Corresponding curves in the source plane are called *fold caustic* (or just *caustics*). They are connected at *cusps* as seen in Fig. 4. When a point source crosses a caustic, a pair of point-like images is created, which are called *critical images*. The two images have opposite parity. The point-source magnification of these two images is infinite on the caustic ($J = 0$), and follow a generic behavior in its vicinity (Schneider & Weiss 1986): for a point-source at a distance a perpendicular to the tangent of a fold caustic, the magnification of the two critical images is equal and behaves as $\mu \propto 1/\sqrt{a}$ (Schneider & Weiss 1986).

When the source is in the vicinity of a cusp, the singularity is more severe (e.g. Zakharov 1995) and the magnification behaves as $1/a$, where a is the distance to the cusp along the symmetry axis.

Since the magnification of critical point sources satisfies $J = 0$, from Eq. (13), Eq. (14) and the fact that $|a|^2 = 1$ implies $a = e^{i\phi}$, this is equivalent to

$$\frac{\partial \zeta}{\partial \bar{z}} = \sum_{i=1}^N \frac{q_i}{(\bar{z} - \bar{z}_i)^2} = e^{i\phi}, \quad (24)$$

where ϕ is an arbitrary parameter. This equation introduced by Witt (1990) is of great interest, since it provides a simple analytic equation that allows to compute the caustics even when a large number of lenses is involved. Critical lines and caustics are obtained by solving Eq. (24) for all $\phi \in [0, 2\pi]$.

In the original publication, ϕ was introduced as an *ad hoc* parameter, but it actually has a geometrical signification. In fact, Cassan (2008) found that there exists a relation between the derivatives of ζ and z relative to ϕ , where ϕ is considered as a curvilinear abscissa along the caustic line:

$$\frac{d\zeta}{d\phi} = \frac{dz}{d\phi} + e^{i\phi} \frac{\overline{dz}}{d\phi}, \quad (25)$$

which leads to $d\zeta/d\phi = e^{i\phi} \overline{d\zeta}/d\phi$. Geometrically, $d\zeta/d\phi$ represents a tangent vector to the caustic line, and $\overline{d\zeta}/d\phi$ is its image by horizontal symmetry. ϕ is then the oriented angle between these two vectors, and $\phi/2$ is the angle between the tangent to the caustic and the horizontal axis, with a jump of π when the point on the caustic passes a cusp.

Critical lines, caustic curves and cusps properties have been extensively studied by many authors (e.g. Cassan 2008; Han 2006; Chung et al. 2005; An 2005; Gaudi & Petters 2002; Petters et al. 2001; Erdl & Schneider 1993). In the case of a single lens, the critical line is the Einstein ring and the caustic is reduced to a point at the lens position. In the case of N point masses, the number of cusps is always even, and the number of closed critical curves cannot exceed $2N$ (Rhie 2003).

Binary (planetary) lenses

The binary-lens model is of great importance, because it provides a very good approximation of a lensing planetary system, even with multiple planets. In fact, although it accounts for only two bodies, in many cases the superposition principle holds. The binary-lens equation reads

$$\zeta = z - \frac{1}{1+q} \left(\frac{1}{\bar{z}} + \frac{q}{\bar{z} + d} \right), \quad (26)$$

where the more massive body is chosen to be at the origin of the coordinates system and the companion at coordinates $(-d, 0)$. For planetary lenses ($q \ll 1$), the second term can be seen as a small correction of the lens equation. The binary-lens equation leads to 5 or 3 solutions, depending on whether the source lies inside or outside a caustic respectively. The point-source magnification is

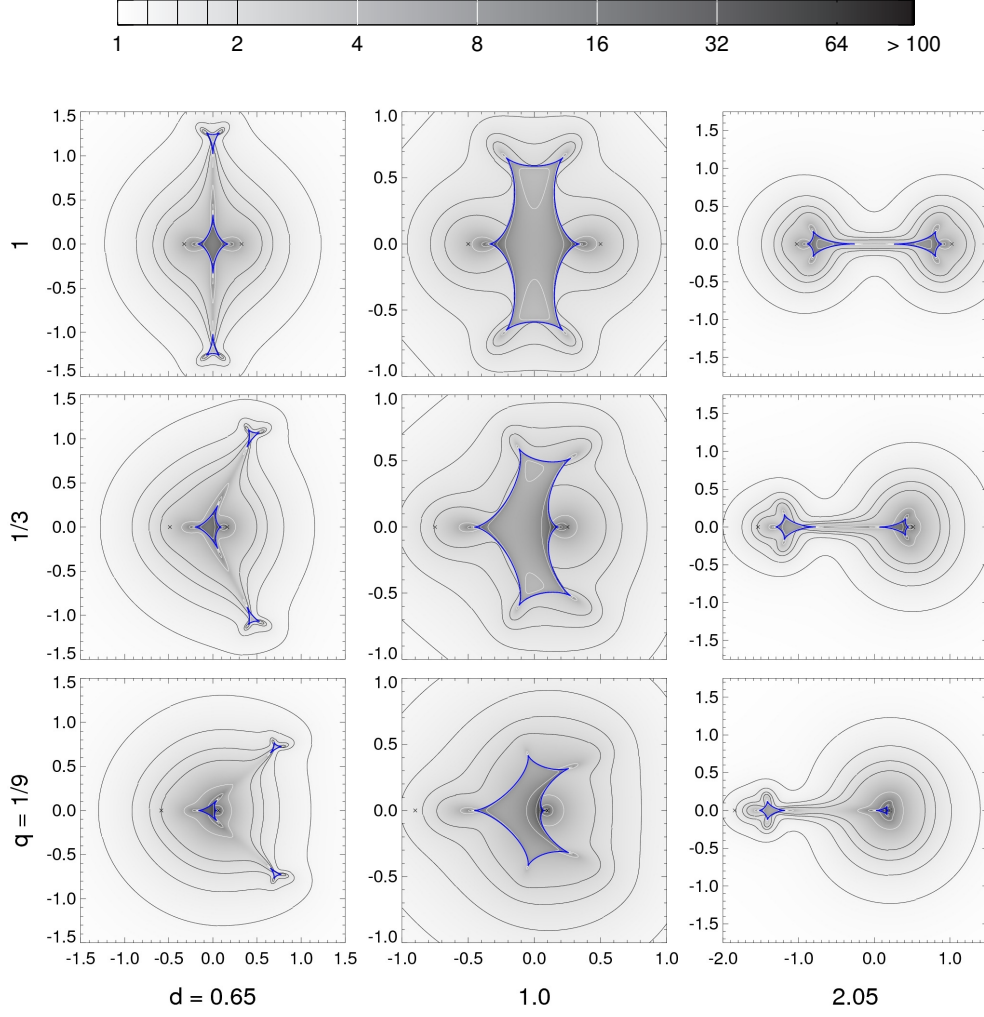


Figure 4: Binary-lens magnification patterns for different separations d (columns) and mass ratios q (rows). The gray scale indicates increasing magnifications from light to dark, while solid lines are iso-magnification contours. The blue lines are caustics (where the point-source magnification diverges) which are connected at cusps. Caustics encompass regions of highest magnification (figure from Pejcha & Heyrovský 2009).

computed from Eq. (14) for each of the images $z^{(k)}$. Amongst particularly interesting properties, Witt & Mao (1995) found that the sum of the 5 images times their respective parity is 1, thus leading to interesting numerical failure tests in computing the magnification. They also found that the magnification inside the caustics is always greater than or equal to 3, whatever the binary-lens configuration.

Typical point-source magnification patterns are presented in Fig. 4 for binary lenses with different (d, q) configurations, and example of point-source light curves are shown in Fig. 5. While the general shape of the light curve can provide information on the underlying binary-lens configuration, such as caustic crossings (short-lasting spikes), only a detailed analysis can reveal the true configuration.

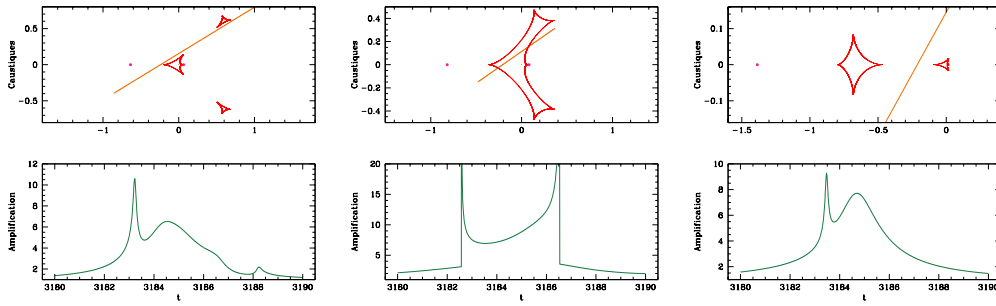


Figure 5: Caustic crossing source trajectories (upper panels) and corresponding light curves (lower panels) for the three binary-lens caustic topologies: close binary (left), intermediate or resonant binary (middle) and wide binary (right). The pink dots mark the positions of the two point-lens components, the caustic lines are drawn in red and the source trajectories are the orange solid lines. The resulting light curves (in green) can hardly be attributed by eye to any of the caustic topology, however, caustic-crossing features are easily recognized as short-lasting brightening episodes (figures from Cassan 2005).

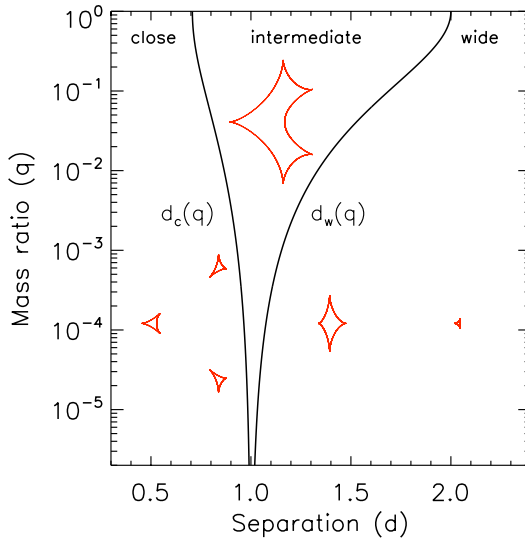


Figure 6: The red curves draw binary-lens caustics curves, which exist in three topologies: close (left, here $d = 0.8$, $q = 10^{-2}$), intermediate or resonant (center, $d = 1$, $q = 10^{-2}$) and wide (right, $d = 1.6$, $q = 10^{-2}$). The bifurcations between these regimes are marked by the solid black lines. Caustics close to the primary lens (greater mass) are diamond-shaped, central caustics, while the others are triangular- or diamond-shaped secondary caustics (figure from Cassan 2008).

Binary-lens caustics exist in three different topologies which solely depend on d and q , as shown in Fig. 6. In the *close binary* case, there exists three caustics, one diamond-shaped *central caustic* located on the horizontal axis, and two triangular off-axis *secondary* (or *planetary*) caustics (on the left in the figure). In the *intermediate* case (in the center of the figure), there is only one six-cusps *resonant* caustic, while in the *wide binary* case there are two caustics (central and secondary), both located on the horizontal axis (on the right in the figure). From catastrophe theory arguments, Erdl & Schneider (1993) found formulae that relate d and q at the transition between different topologies, from close to intermediate:

$$d_c^8 = \frac{(1+q)^2}{27q} (1-d_c^4)^3, \quad (27)$$

and intermediate to wide:

$$d_w^2 = \frac{(1+q^{1/3})^3}{1+q}. \quad (28)$$

The corresponding functions $d_c(q)$ and $d_w(q)$ are plotted as solid black lines in Fig. 6. For small planetary mass ratios ($q \ll 1$), resonant caustics exist only for a small range of separations. Nevertheless, intermediate caustics are much more often detected than would be expected from this theoretical consideration. The reason is that the area of a resonant caustic is much higher than that of a central or planetary caustic, and this dramatically increases the probability that a source crosses such a caustic. Wide and close central caustics with respective separations d and $1/d$ resemble more and more each other for decreasing mass ratios q , leading to the well-known *wide-close degeneracy* (Dominik 1999; Erdl & Schneider 1993). The wide binary secondary caustic has a much greater area than the central caustics for a given q ; this is because the size of the central caustics shrinks as q when $q \rightarrow 0$, while the secondary caustic only shrinks as $q^{1/2}$ (e.g. Han 2006; Chung et al. 2005). Hence, secondary caustics have a higher probability to be crossed by a source during a microlensing survey. In reality, it is not easy to detect a secondary caustic deviation, because it is impossible to predict when it will occur. In contrast, in central caustic-crossing events planetary deviations occur at the peak of the light curve, and dense observational cadence can be planned. Planet detections that are due to secondary caustic crossings are called *planetary caustic events*. Those detected *via* central caustic crossing are *central caustic events*. They lead to two different follow-up observing strategies, as detailed later.

4. Light curve anomalies

Around 10% of microlensing events display *anomalies*, which are deviations from standard point-source point-lens light curves. Several effects can distort a microlensing light curve, which have to be distinguished from systematic errors in the data. Here we provide a concise overview of the most important causes for light curve anomalies.

Blending flux

In general, the observed flux $F(t)$ is not proportional to the magnification $\mu(t)$ (Alcock et al. 2001), because sources of light other than the magnified flux of the source star are collected by the detector. For example, it is impossible to disentangle in a single observation the flux of the source F_S from the flux of the lens F_L , because the lens-source alignment is always too small ($< 10^{-4}$) to be resolved. Furthermore, typical microlensing fields towards the Galactic bulge are very crowded (Fig. 7), and the PSF includes light from neighboring stars which also contribute additional light. This flux from unrelated stars plus the flux from the lens is called the *blend flux* F_B , or *blending*. The total flux then reads:

$$F(t) = A(t) F_S + F_B. \quad (29)$$

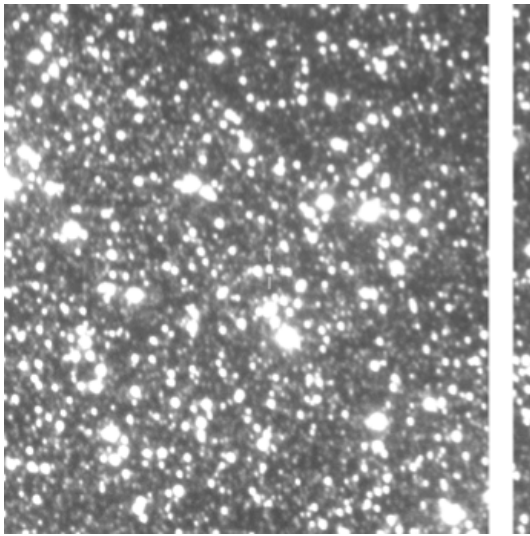


Figure 7: A typical image of a Galactic bulge microlensing event (here the finding chart of OGLE 2005-BLG-390). The image size is $2' \times 2'$, East is up and North is to the right. The position of the microlensing event is indicated by the white cross at the center of the frame (courtesy OGLE collaboration).

When many telescopes are observing in different filters, every single light curve introduces an additional pair of parameters (F_S, F_B). Hence, apart from the parameters defining the lensing system and the source trajectory (that we will refer to as *model parameters*), any model involves $2N$ additional *flux parameters* accounting for the N data sets involved. This subsequent increase of the number of parameters can be critical. Fortunately, an easy way to deal with the problem is to treat independently the $2N$ flux parameters as follows. For a given set of model parameters and a light curve $F^{(j)}(t_k)$ observed by telescope $1 \leq j \leq N$, it is clear from Eq. (29) that $F_S^{(j)}$ and $F_B^{(j)}$ can be straightforwardly computed by a least square fit to the data, given $A(t_k)$ computed from a chosen set of microlensing model parameters (which are those that have to be optimized).

Multiple lenses

The range of binary-lens separations for which the sensitivity to lens companions is highest is called the *lensing zone* and approximately spans $0.6 \leq d \leq 1.6$ (Wambsganss 1997). Cases of triple lens configurations have been reported in planetary events (e.g. Gaudi et al. 2008).

When the secondary caustics of multiple lenses are well separated, the superposition principle holds, as shown in the example triple-lens configuration in

the left panel of Fig. 8. Otherwise, the combination of the caustics is strongly non-linear as shown in the right panel. The shape of the central caustic, although always a non-linear combination of the different central caustics of the companions, is clearly dominated by the central caustic of the biggest body.

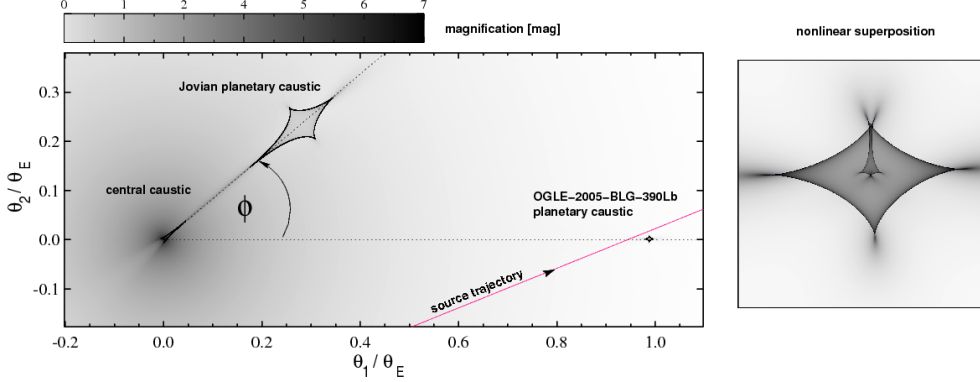


Figure 8: The left panel of the figure displays a magnification map of a triple lens system configuration, consisting of a host star at the origin and two planets. On the left panel, the secondary caustics of the two planets are far enough, and can be accounted for by a simple superposition principle. On the right panel, the caustics are too close and a complex caustic pattern is created (figure from Kubas et al. 2008).

Finite source effects

When the source approaches a caustic, it cannot be considered as point-like anymore and deviations from a point-source light curve are clearly detected. In case it is possible to measure the source size in θ_E units, an independent relation between the source physical radius R_\star (or the angular radius ρ_\star , in mas), the source distance D_S and θ_E can be written:

$$\rho = \frac{\rho_\star}{\theta_E} = \frac{R_\star}{D_S \theta_E}. \quad (30)$$

R_\star can be estimated from the color and the magnitude of the source using a calibrated color-magnitude diagram and an estimate of D_S (usually ~ 8 kpc). Otherwise, ρ_\star can be derived from surface brightness relations (Kervella & Fouqué 2008). Since θ_E depends on M and D_L , Eq. (30) can be understood as a mass-distance relation for the lens.

Parallax effects

The motion of the Earth around the Sun causes the alignment between observer, lens and source to differ from an otherwise rectilinear apparent motion of the source relative to the lens. Parallax effects have been detected in many microlensing events. When the relative parallax in Einstein units $\pi_E = \pi_{\text{rel}}/\theta_E$ is measured, it leads to the following relation between θ_E and the lens mass M :

$$\pi_E = \frac{\pi_{\text{rel}}}{\theta_E} = \frac{\theta_E}{\kappa M}, \quad (31)$$

which is another independent mass-distance relation. Consequently, if both ρ and π_E are measured, the lens mass M and distance D_L are determined exactly (e.g. Kubas et al. 2005). In practice, in microlensing models parallax is parametrized by two parameters $\pi_{E,E}$ (East) and $\pi_{E,N}$ (North) in a geocentric formalism (An et al. 2002; Gould 2004) that distinguishes the fact that Earth motion around the Sun in the East-West direction has more effect than in the North-South direction. The parallax parameter π_E then becomes a vector with coordinates $(\pi_{E,E}, \pi_{E,N})$. Several subtle degeneracies can affect the model parameters when parallax effects are introduced in a model. The “constant motion degeneracy” (Smith et al. 2003) show that an almost identical light curve is obtained when $u_0 \rightarrow -u_0$ and $\alpha \rightarrow -\alpha$. Another important degeneracy is the “jerk parallax degeneracy” (Gould 2004), resulting from an apparent acceleration of the source motion. Gould (2004) introduced a decomposition of the vector π_E into two different coordinates $(\pi_{E,\parallel}, \pi_{E,\perp})$, with $\pi_{E,\parallel}$ the direction to the position of the Sun at the peak of the event, projected onto the plane of the sky. These parameters are almost uncorrelated. In most cases, $\pi_{E,\parallel}$ is much better constrained than $\pi_{E,\perp}$.

Finally, *terrestrial* parallax effects can be detected as well (Gould et al. 2009; Holz & Wald 1996; Hardy & Walker 1995). In this case, the rotation of the Earth itself introduces a difference in the timing of the data sets gathered at different longitudes, that can be exploited to constrain a lens mass-distance relation. It is also one of the very few possibility to allow a direct measurement of the mass and number density of isolated dark low-mass objects, such as old free-floating planets or brown dwarfs (e.g. Gould & Yee 2013).

Binary source and "xallarap" effects

When the source star has a massive enough but unseen companion, its orbital motion can be detected in the light curve. The modeling is almost identical to annual or terrestrial parallax effects.

Which effects should be included ?

Not all effects mentioned here can be observed at the same time; this depends on the characteristics of the microlensing event. For example, it is unlikely that a short event displays parallax effects, and xallarap is usually exclusive from parallax effects (which can sometimes lead to ambiguities in the parameters of the model).

B. Events follow-up strategy

1. The "alert and follow-up" observing strategy

Microlensing events happen as a very rare and stochastic process of a chance alignment between a background star and a foreground star. The quantity that quantifies the probability that any given star is being lensed by a foreground massive object (the lens) at any given time is called the *lensing optical depth*, τ . A background star is considered to be lensed when it lies within the Einstein

radius of a foreground object. The probability of a microlensing event is highest when telescopes are pointed to regions of the sky where the density of background stars is highest, *i.e.* in the direction of the Galactic bulge, and preferably in areas less affected by strong extinction due to interstellar dust such as the Baade's window (Fig. 7). Precise calculations (e.g. Han & Gould 1995) and measurements (e.g. Sumi et al. 2006; Afonso et al. 2003) of the optical depth lead to a typical probability of $\tau \sim 10^{-6}$, *i.e.* one star out of a million is lensed at any given time towards the Galactic bulge. The *event rate* Γ , which quantifies the rate at which a given background star is lensed by a foreground star (e.g. Kiraga & Paczynski 1994), is the most interesting quantity from an observational point of view. For a typical microlensing event duration of $t_E \sim 20$ days and $\tau \sim 10^{-6}$, a typical value for the event rate is $\Gamma \sim 10^{-5} \text{ year}^{-1}$. The consequence of this very low rate is that the detection of microlensing events requires monitoring a very large number of background stars, $\sim 10^8$ in current microlensing surveys. Interestingly, it can be noted that microlensing is the only method that is not limited in the number of potential targets.

Typical durations of microlensing events range from a few days to a few weeks or months, with a median value of $t_E \sim 20$ days. Planetary deviations affecting single-lens-like light curves are much shorter, lasting from days to few hours. Hence microlensing poses the challenge of monitoring a large number of stars at high cadence. With classical 1m-class telescopes that have been in operation for microlensing observations since the beginning of the 1990s, the dense follow-up of such a high number of stars with a single telescope was impossible because their field-of-view was too narrow ($< 1/4 \text{ deg}^2$). Many pointing of the telescopes in different line-of-sights are required, which dramatically slow down the data acquisition rate. Furthermore, storage of large data sets has long been a major barrier, and was solved only recently. To overcome the problem, Gould & Loeb (1992) advocated for a two-stage observing strategy: survey telescopes monitor at low cadence (one point per night, or every few hours) a large number of stars, while networks of narrow-angle telescopes distributed longitudinally in the Southern Hemisphere focus their resources on a limited sample of selected events, with much higher data collecting rate (down to a few minutes interval).

Historical survey collaborations include EROS (*Expérience de Recherche d'Objets Sombres*, Aubourg et al. 1993), DUO (*Objets Invisibles du Disque*, Alard & Guibert 1997), MACHO (*the Massive Astrophysical Compact Halo Object project*, Alcock et al. 1993), OGLE (*the Optical Gravitational Lensing Experiment*, Udalski 2003) and the MOA (*Microlensing Observations in Astrophysics*, Bond et al. 2001) collaborations. Currently, OGLE (started in 1992) and MOA (started in 1995) are pursuing their survey. Both have upgraded their instruments and alert systems over the course of time. From a 0.6 m telescope at Mt John University Observatory (New Zealand), in 2003 MOA II upgraded to a 1.8 m telescope with a wide field-of-view camera of 2.2 deg^2 . In its first three years of operations (1998-2000), OGLE detected 40 – 80 alerts with its 1.3 m telescope in Las Campanas (Chile). It then improved its strategy to increase the number of alerts steadily from 350 in 2002 to 650 alerts in 2009. In its current setup, OGLE IV has upgraded to a new wide-field imager of 1.4 deg^2 , and now detects around 2000 microlensing events per year.

Follow-up collaborations started operations with the goal of monitoring at high cadence individual microlensing events alerted by survey collaborations. These round-the-world networks of telescopes perform an almost continuous observation of microlensing events, and can react to light curve anomalies on time-scales of a few minutes. Currently, follow-up collaborations include PLANET (Albrow et al. 1998, start in 1995) which was joined by RoboNET in 2003, μ FUN, MiNDSTeP and LCOGT. While microlensing event baseline magnitudes can be faint, as shown in the histogram of OGLE 1998-2007 baselines presented in Fig. 9, magnification factors are large enough that peak magnitudes can commonly reach $I = 16$ or 15 for the faintest objects, which allows the use of small-aperture telescopes to observe those sources. Hence, microlensing networks usually involve 0.6 to 2 m class telescopes.

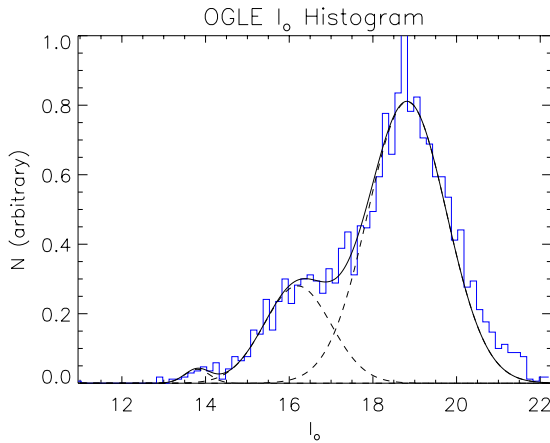


Figure 9: Histogram of baseline magnitudes of microlensing events detected by OGLE in 1998-2007 (in blue). The black solid line is a tentative fit to the histogram, and results from the sum of three sub-populations of source stars (dashed Gaussian curves): main-sequence, giant and super-giant stars.

In practice, PLANET follow-up observations work as follows. From the data base of events alerted by OGLE and MOA (alerts are public, as was recommended by B. Paczynski), a selection of ~ 20 events are monitored at any time, at a rate of one point per night up to one point every few minutes. Data reduction is performed in real time and data sets from all telescopes are uploaded on a central computer located at the Institut d’Astrophysique de Paris. A web-based tool, the “PLANET plotter”, is used to display all data collected, together with a fitted single-lens model. On the same web page, a “homebase astronomer” updates the list of events and adapt the recommended priority and observing rate accordingly. A daily feedback is sent to the observers, who also fill daily night reports. In the case of a light curve anomaly detected by one of the telescope in the network, the observer immediately contacts the “homebase” who may circulate an internal alert to other observing sites, or deliver a public alert to other collaborations if the anomaly is confirmed. It is very common that observers directly contact by phone the astronomers in duty at the telescope that is coming next in longitude to ensure continuous coverage.

Many numerical tools have been developed and implemented to help predict light curve parameters and detect alerts. For example, Bayesian algorithms of early estimation of microlensing event parameters (e.g. Albrow 2004) are implemented on the PLANET internal web pages to help prioritize microlensing light

curves, based on the large data base of events light curves gathered by PLANET. Other tools are dedicated to detect light curve anomalies (Horne et al. 2009; Dominik et al. 2007) or model complex anomalous signals (e.g. Cassan 2005).

2. Two detection channels

The original microlensing observing strategy in 1995 was to continue the follow-up of a microlensing event until the source exits the Einstein ring, which happens at magnification of $A = 1.34$. The basic idea of this strategy was to try to detect a secondary caustic crossing. This strategy, however, required substantial observing resources, since the date of a potential deviation was essentially unpredictable, and a continuous and intense monitoring of all lenses was mandatory. Shortly after the first observing seasons, however, a study by Griest & Safizadeh (1998) challenged this simple follow-up strategy. The authors realized that in high-magnification events, the probability that the source crossed a central caustic was very high (even reaching 100%), even if the central caustic is smaller than the secondary caustic. The central caustic is in fact located close to the primary lens, and the source trajectory in a high-magnification event is very likely to cross the caustic at the peak of the event. Monitoring high-magnification events is also easier, since the peak of the event can usually be predicted.

In summary, microlensing planets can be discovered *via* two detection channels: (1) the *high-magnification* or *central caustic* channel, which consists in detecting high-magnification events, predicting their peak date and maximum magnification, and subsequently planning continuous observations around the peak (the highest the peak magnification, the shortest its duration; hundreds of points in a night can be collected); (2) the *low-magnification* or *planetary caustic* channel, which relies on a continuous monitoring of microlensing events while the source still lies in the lensing zone (*i.e.*, $0.6 - 1.6 \theta_E$). Planets have been detected in both channels. Today, these two channels tend to merge into an homogeneous strategy that takes advantage of new generation of robotic, wide-field imagers that allow a continuous monitoring of a large number of microlenses at the same time (section IV).

3. Real-time data reduction and modeling

Since a microlensing event is a transient phenomenon, the success of the project strongly relies on the availability in real time of the data, the estimation of the underlying single-lens model to spot light curve anomalies, and as much as possible on the characterization of the anomaly to tell whether the event is planetary or not (or can lead to interesting science).

From 1995 to 2005, PLANET data were reduced online with a dedicated photometry pipeline based on PSF fitting, using the DoPHOT technique (Schechter et al. 1993). Data were reduced at the telescope and transferred to a central computer. In 2006, PLANET started to implement image subtraction techniques (Alard & Lupton 1998), also called difference image analysis (DIA). In this technique, an image of the field is subtracted from a reference image, after a proper

astrometric calibration. All constant objects thus disappear while variable objects can be analyzed. The PLANET pipeline was built around the software ISIS developed by Alard (2000). The pipeline was designed to process all newly incoming images, choose a reference template image if not yet done, subtract all images and build up the archive and light curve.

In 2008, Bramich (2008) proposed to replace the standard DIA technique (which used a linear combination of basis functions) by a numerical convolution kernel, *i.e.* a kernel composed of a discrete pixel array. Since the kernel is directly based on pixel patterns and not on mathematical functions, there is no need to manually choose the basis function, which greatly simplifies the use of DIA. Furthermore, there is no requirement that the numerical kernel be built at the origin of the coordinates, which naturally corrects for a certain degree of misalignment. It also avoids image resampling. This algorithm has been adapted into the PLANET photometry pipeline (Albrow et al. 2009) that is currently in use.

When data are available, a single-lens model is automatically fitted to the data, in order to check for anomalies. However, when only very few data are available on the rising wing of a microlensing event, even a single-lens model can be poorly constrained. Very large and unrealistic peak magnifications are then usually predicted; Bayesian estimation can help predicting more realistic model parameters in this critical phase of monitoring (Albrow 2004).

Once an anomaly is detected, complex modeling is required to understand the true nature of the microlensing event. This is done by individual modelers, who share in real time the results of their modeling work. Fully automated fitting codes are not yet ready, because many aspects are still challenging. Nevertheless, recent progress are very promising signs that automated softwares may soon be available (section IV), in particular in combination with robotic telescopes.

4. Further observations

While a photometric microlensing event itself does not repeat, many further observations are in most cases possible both during and after the event. Color-magnitude diagrams (CMD) obtained in real time provide important information on the source properties and extinction along the line-of-sight, because red clump giant stars, which have a well-defined location in the de-reddened CMD (Paczynski & Stanek 1998), are usually clearly identified in the CMD. Microlensing events are sometimes observed in non-standard filters which have slight differences from one another. Gould et al. (2010a) proposed a very efficient method to use this apparent “drawback” as a way to calibrate multi-site light curves, which yield the source color independently from the model. High-resolution images are also gathered at VLT using NACO spectrograph. Data are calibrated to 2MASS magnitudes thanks to IRSF data (South Africa) that make the link between 2MASS and NACO (Kubas et al. 2012). Calibrated CMDs in the infrared bands JHK_s are then derived (Fig. 10). As mentioned earlier, HST data can also be used to detect a separation between the lens and source a few years after the event is over, due to relative lens-source motion (Bennett et al. 2006). Space-based

parallax can also be obtained from spacecrafts, such as Deep Impact (Muraki et al. 2011) or Kepler (Gould & Horne 2013), thanks to the long base between satellite and Earth observatories.

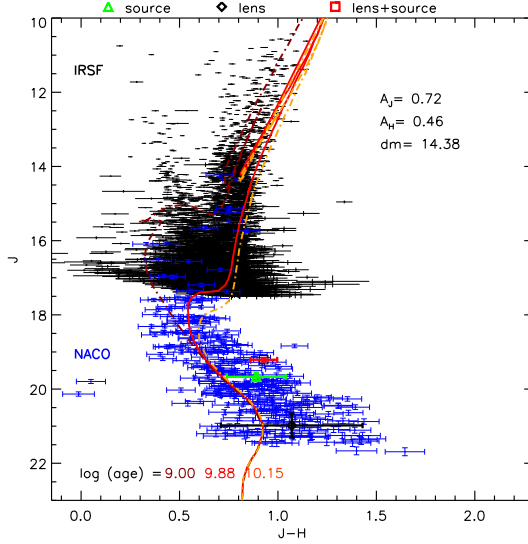


Figure 10: A 2MASS-calibrated color-magnitude diagram of VLT/NACO data of the MOA 2007-BLG-192 field in J and H infrared filters, using IRSF data (figure from Kubas et al. 2012).

These further measurements provide independent information that help break model degeneracies or ambiguities. When telescope time is granted, they are routinely performed for most of the top events of an observing season.

C. Astrophysical applications

Microlensing was proposed by Paczynski (1986) as an original tool to detect dark objects and explore the hidden mass content of the Galaxy. The microlensing technique was first used to probe an hypothetical population of dark, massive, baryonic objects in the halo of the Milky Way, called MACHOs (MASSive Compact Halo Objects), that could account for the dark matter content of the Galaxy. The conclusion of this study spanning 20 years of observations (Tisserand et al. 2007; Wyrzykowski et al. 2011) is that at most $\sim 2\%$ of halo objects is found in the form of MACHOs. Microlensing has many other astrophysical applications. As advocated by Mao & Paczynski (1991), microlensing is a unique tool to probe the Galactic structure, revealing populations of otherwise unseen objects, such as brown dwarfs and extrasolar planets. Important informations have been obtained on red clump giants (standard candles to measure distances), extinction maps towards the bulge, proper motions of stars, Galactic bar structure, disk and bulge mass functions, or on the stellar atmospheres of bulge red giants.

1. Probing the stellar atmospheres of Galactic bulge giants

Apart from the Sun, stellar limb darkening (apparent variation of brightness from centre to limb) can be measured by very few observational techniques: eclipsing binaries, transiting extrasolar planets, interferometry and microlensing. Pho-

tometry and low-resolution spectroscopy of stars usually yield spectral types and other general informations, but much of the detailed properties of the structure of stellar atmospheres is lost in the disc-integrated flux. Measurements that can spatially resolve the disk of stars are rare, but provide unique opportunities for testing stellar atmosphere models. These are usually calculated for a broad range of stellar types (e.g. MARCS, Gustafsson et al. (2008); ATLAS, Kurucz (1992); Plez et al. (1992)) and a range of optical depths, and predict limb darkening profiles.

In order to be used for these purposes, the event should feature a source that transits a region of caustics, where the magnification gradient is not uniform over the source's disk. Point-like caustics crossing in single lenses or caustic crossing in binary lenses hence provide unique tools to study distant stellar atmospheres. Furthermore, these stars are magnified, which allow to use high resolution spectroscopic instruments. While most methods probe nearby stars, microlensing is the only technique that can probe stellar atmospheres of stars at several kpc from us.

Stellar limb-darkening coefficients

Early works have pointed out the great sensitivity of microlensing light curves to stellar limb darkening (in particular, Witt 1995; Loeb & Sasselov 1995), although it was first proposed as a way to break microlensing model degeneracies. After these pioneer studies, microlensing was quickly envisaged as a specific tool to study stellar atmospheres (e.g. Sasselov 1996; Hendry et al. 1998; Gaudi & Gould 1999), in particular for Galactic bulge red giants (e.g. Heyrovský et al. 2000). Microlensing measurements of limb-darkening coefficients have been obtained for main-sequence to giant stars. MACHO 1998-SMC-1 was the first event to be analyzed (Albrow et al. 1999; Afonso et al. 2000). It involved a metal-poor A6 dwarf source located in the Small Magellanic Cloud. Although photometric data were taken in five filters, comparison with atmosphere models could not be achieved since very little data existed for such stars. The first microlensing limb-darkening measurement for a Solar-like star (a F8-G2 main-sequence turn-off star) was reported by Abe et al. (2003) in a very high-magnification event, MOA 2002-BLG-33. A good agreement between the measured limb-darkening coefficient in the I band and the stellar model prediction was found. Binary-lens caustic-crossing event OGLE 1999-BLG-23 offered a good opportunity to measure limb-darkening coefficients of a late G (or early K) sub-giant (Albrow et al. 2001). Here again, theory and measurement agreed fairly well in the I and R filters.

Red giant stars are the easiest targets for microlensing observations, because they are bright and their light suffers less from interstellar extinction. Late M giants are of special interest because they test atmosphere models at the lower end of available stellar models. Limb-darkening effects were reported in the light curve of MACHO 95-30, which source was a late M4 red giant Alcock et al. (1997). The intrinsic variability however precluded any useful measurement. Albrow et al. (1999) derived I and V limb darkening coefficients for the K2 giant source star of MACHO 1997-BLG-28 (involving a cusp crossing), and found a

good agreement with model predictions (although at low confidence level), and similarly for MACHO 1997-BLG-41 (Albrow et al. 2000), which involved a late G5-8 giant crossing two caustics. Microlensing event EROS BLG-2000-5 provided the first very good opportunity to probe at high precision the limb darkening of a K3 giant, in five filters (Fields et al. 2003). The limb darkening coefficients in the V , I , and H filters were found to be discrepant from atmosphere models, probably due to inadequate physics in the stellar model. Real-time spectroscopic observations at high resolution also revealed a clear variation in the shape of the $H\alpha$ line during the microlensing event.

The microlensing binary-lens event OGLE 2002-BLG-069 (Cassan et al. 2004; Kubas et al. 2005) featured a caustic crossing entry at high photometric precision, which allowed to predict the date of the caustic exit a few days in advance. Intense photometric and spectroscopic monitoring could be achieved. The source star was a G5 Galactic bulge giant, for which I and R bands limb-darkening were measured. The linear limb-darkening model was consistent with the data, while a state-of-the-art LTE PHOENIX atmosphere model did not match well the observations. A detailed analysis revealed that the discrepancy could be explained by the lack of a proper implementation of the chromosphere properties (Cassan et al. 2004).

Event	Type	Source characteristics			Measured LLDC	ATLAS LLDC	ATLAS
		T_{eff}	$\log g$	[Fe/H]	a_1	a_1	a_1 (new fit)
MACHO 1997-BLG-28	K2 III	4250 K	2.0	0.0	0.83 ($\pm 15\%$)	0.65	0.60
MACHO 1997-BLG-41	G5-8 III	5000 K	3.2	-0.2	0.46	0.58	0.53
EROS 2000-BLG-5	K3 III	4200 K	2.3	+0.3	0.54	0.67	0.62
OGLE 2002-BLG-069	G5 III	5000 K	2.5	-0.3	0.60	0.57	0.52
OGLE 2003-BLG-262	K1-2 III	4500 K	2.0	0.0	0.70 \pm 0.13	0.63	0.58
OGLE 2003-BLG-238	K2 III	4400 K	2.0	0.0	0.57 \pm 0.06	0.64	0.59
OGLE 2004-BLG-254	K3 III	4000-4300 K	1.5-2.5	+0.2-+0.4	0.53 $^{+0.04}_{-0.06}$	0.63 (closer)	0.58 (closer)

Table 1: Limb-darkening coefficients for the I -band of published G-K Galactic bulge giants published before 2006. The column ATLAS LLDC is from Claret (2000), whereas the last column is a new fit to ATLAS model atmosphere intensities. The ATLAS parameter values given here are the closest to the measured ones (table from Cassan et al. 2006).

High-cadence observations were obtained for OGLE 2004-BLG-254 (Cassan et al. 2006), which involved a K3 giant microlensed by a single star. Spectroscopic data was obtained from UVES at VLT at ESO’s Paranal Observatory and were used to determine precisely the star’s spectral type. Linear limb-darkening coefficients in the I and R filters were measured and discussed with other published measurements involving G-K giants (Tab. 1). Theoretical limb-darkening coefficients using a new ponderation of the ATLAS models (Heyrovský 2007) were also compared to Claret (2000)’s widely-used coefficients. After taking into consideration technical effects in microlensing light curves, as discussed in Cassan et al. (2006), only EROS 2000-BLG-5 and OGLE 2003-BLG-238, both K giants, appeared to disagree with Claret (2000) predictions. Interestingly, coefficients obtained using the new ponderation (“new fit” in Tab. 1) are much closer to the observed values, and it is also the case for the other events.

Zub et al. (2011) performed a detailed analysis of OGLE 2004-BLG-482

(in particular, the stability of the model parameters when data sets are included or removed), which involved a cool M3 (or slightly later) red giant star ($T_{\text{eff}} = 3667 \pm 150$ K). The light curve is shown in Fig. 11. The source star was resolved by a single microlens, and linear limb-darkening coefficients were measured in the I and R filters. High-resolution VLT/UVES spectra (obtained on Target of Opportunity time at ESO) allowed for the determination of the spectral type of the source. A very good agreement was found between the measurements and the predicted linear limb-darkening coefficients computed from ATLAS stellar atmosphere models. In addition, a principal component analysis (PCA) of ATLAS limb-darkening profiles was performed, which yielded a good fit to the observations.

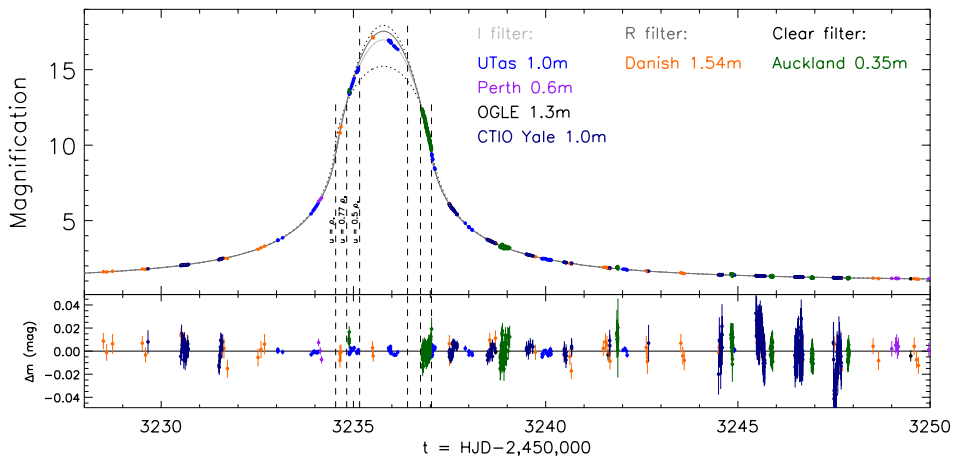


Figure 11: Light curve and fit residuals of OGLE 2004-BLG-482, showing PLANET, OGLE and μ FUN data. The two gray solid lines in the upper panel are the best-fit model for the I and R filters respectively. The dotted curves correspond to the two extreme cases: uniformly bright source (lower curve) and maximal limb darkening (upper curve). The vertical lines marked $u = \rho$ indicate when the lens is located at the limb of the source. All curves intersect at $u = 0.77 \rho$ (figure from Zub et al. 2011).

Limb-darkening coefficients were also measured in other events, such as OGLE 2003-BLG-238 (Jiang et al. 2004) and OGLE 2004-BLG-262 (Yoo et al. 2004), which involved early K1-2 giants, but were not suitable to draw robust conclusions on limb darkening analysis. Choi et al. (2012) selected nine microlensing events sensitive to limb darkening: MOA 2007-BLG-176, MOA 2007-BLG-233 / OGLE 2007-BLG-302, MOA 2009-BLG-174, MOA 2010-BLG-436, MOA 2011-BLG-093, MOA 2011-BLG-274, OGLE 2011-BLG-0990 / MOA 2011-BLG-300, and OGLE 2011-BLG-1101 / MOA 2011-BLG-325. Dense observations of OGLE 2008-BLG-290 provided accurate measurements of the limb darkening coefficients of a Galactic bulge K giant (Fouqué et al. 2010), in six photometric bands. A discrepancy was found between the measurements and the stellar model predictions, possibly originating from an inadequate estimation of the source’s temperature as determined from its photometric color.

Stellar tomography at high spectroscopic resolution

A spectroscopic monitoring at high resolution can resolve individual spectral lines at different positions on the stellar disc. Real-time photometric monitoring is required to plan a few days in advance Target of Opportunity high-resolution spectroscopic observations. Castro et al. (2001) managed the first successful attempt to obtain two spectra with KECK HIRES on EROS 2000-BLG-5, but missed the limb where the effects are stronger. Albrow et al. (2001) also observed this event, but at low spectral resolution. Afonso et al. (2001) used a toy model that reproduced the main features of the variation of the shape of $H\alpha$, and found an excess flux possibly due to chromospheric emission.

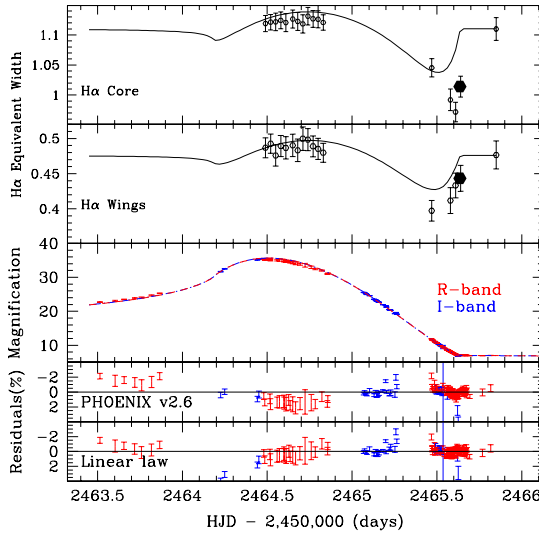


Figure 12: The two upper panels show the equivalent width of UVES spectra as a function of time (data points), as well as the predicted equivalent width based on the photometric model and synthetic spectra computed from PHOENIX stellar atmosphere models (solid curves). The middle panel shows the photometric light curve in I and R using linear limb darkening laws, and the two lower panels are the fit residuals (figure from Cassan et al. 2004).

OGLE 2002-BLG-069 provided the first opportunity to monitor the caustic exit of a binary microlensing event (Cassan et al. 2004) at high spectroscopic resolution. Photometric data were gathered by PLANET and OGLE networks, while spectroscopic data were obtained with UVES on the VLT. The source star was a G5 giant in the Galactic bulge, for which an appropriate stellar atmosphere model was generated by the PHOENIX v2.6 code. Synthetic magnified spectra were computed and compared to UVES data. The variation of the equivalent width of $H\alpha$ during the caustic crossing is shown in Fig. 12. While model and observations agree in the gross features, discrepancies remain at the limb, which can naturally be attributed to a chromosphere that is not taken into account by the model. This is further confirmed by an extra $H\alpha$ emission that is detected in spectra taken at the limb of the star. Last but not least, OGLE 2002-BLG-069 is the very first case of an observation of the chromosphere of a giant star in the Galactic bulge.

Microlensing is thus a very efficient tool to measure limb-darkening coefficients for stars other than the Sun, and can even provide a direct tomography of stars when spectroscopic observations at high resolution are possible.

2. Mass and distance of isolated and binary stars

Microensing is a tool to probe the Galactic structure, because it can detect dark or very distant objects that would be otherwise unseen. The most basic microlensing models are affected by a degeneracy of order two, which means that the lens mass and distance cannot be disentangled. Fortunately, if two secondary effects are measured (amongst e.g. finite-source, parallax, xallarap, source rotation, high resolution photometry...), then all physical quantities can be determined.

Isolated stars

Microensing is one of the very few methods that can directly measure the mass of an isolated star, even at distances of several kpc. After MACHO-LMC-5 (e.g. Gould 2004), OGLE 2003-BLG-238 is the second case of the mass of an isolated object determined by microlensing (Jiang et al. 2004). This event was a very bright ($I \simeq 10$) and highly magnified event ($A \simeq 170$), for which parallax and finite-source effects were measured simultaneously. Although the lens mass was not measured very precisely ($M \simeq 0.36 - 1.48 M_{\odot}$), it demonstrated the potential of the technique to measure the mass of unseen stars in the Galactic disk or bulge. Ghosh et al. (2004) analyzed OGLE 2003-BLG-175 / MOA 2003-BLG-45, which displayed obvious signatures of parallax effects, but no sign of finite-source effects (as expected for low-magnification events). Future high-resolution astrometry, when the lens and the source are resolved, will yield the lens-source relative proper motion, and constrain the lens mass. This has been used since for planetary microlensing events. Several other mass measurements were reported, which confirmed that microlensing lens stars are mainly M and K dwarfs. OGLE 2007-BLG-050 (Batista et al. 2009), a very high-magnification event of $A \sim 400$, provided a relatively precise determination the lens mass ($M = 0.50 \pm 0.14 M_{\odot}$) and distance ($D_L = 5.5 \pm 0.4$ kpc). In MOA 2009-BLG-174, Choi et al. (2012) determined the lens mass ($M \sim 0.74 M_{\odot}$) but at much lower precision. Confidence limits on the possible presence of companions to the lens were also computed for a number of events.

Direct single star mass measurements provide unique opportunities to test predictions from Galactic models. Thanks to microlensing events for which parallax was detected, Smith et al. (2005) performed a comparison between a state-of-the-art Galactic model and observations. They found that the fraction of parallax events in the OGLE-II database (a few per cent) was in agreement with model expectations. Furthermore, they estimated that around 1/3 of parallax events were caused by a lens in the Galactic disk and a source in the bulge, another 1/3 by a disk-disk event, and a last 1/3 resulting from bulge-bulge microlensing.

Choi et al. (2012) analyzed several high-magnification events observed between 2004 and 2011 that displayed single-lens, finite-source effects (OGLE 2004-BLG-254, see also Cassan et al. (2006); MOA 2007-BLG-176; MOA 2007-BLG-233 / OGLE 2007-BLG-302; MOA 2009-BLG-174; MOA 2010-BLG-436; MOA 2011-BLG-093; MOA 2011-BLG-274; OGLE 2011-BLG-0990 / MOA 2011-BLG-300; OGLE 2011-BLG-1101 / MOA 2011-BLG-325). Five of these events with

$\theta_E < 0.2$ mas were found to involve very low mass stars or brown dwarf candidates. With $\theta_E \sim 0.08$ mas and $t_E \simeq 2.7$ days, the lens of MOA 2011-BLG-274 could even be a free-floating planet, with no chance to be confirmed, though.

Binary stars

Around 10% of all microlensing events are binary-lens events. A few are planetary or brown dwarf companions to stars, but most are binary stars (Skowron et al. 2007; Jaroszynski et al. 2006, 2005, 2004; Jaroszynski 2002). Binary-lens events provide important insights into the population of Galactic disk's objects, in particular about their mass function. A complete view of stellar multiplicity requires a variety of observational methods, and in fact, compared to other techniques, microlensing has the great advantage not to be biased towards bright objects. Current surveys give more and more attention to monitor and analyze such events.

Binary-lens event OGLE 2002-BLG-069 (Kubas et al. 2005; Cassan et al. 2004) was the second event for which the masses of the two individual components were measured, after EROS-BLG-2000-5 (An et al. 2002). Two models were found to be equally good to fit the data (wide vs. close model degeneracy), but with different plausibility: the preferred scenario implied a standard binary-star lens of total mass $M = 0.51 \pm 0.15 M_\odot$ with a source in the Galactic bulge and a lens in the disk, while the second model implied a very unlikely pair of black-hole mass objects ($M > 126 M_\odot$).

Orbital motion of the two lens components can sometimes be measured in close binary systems (in particular if t_E is long enough). The full parameters of OGLE 2005-BLG-018 were determined this way (Shin et al. 2011): parallax and orbital motion effects were combined in the modeling to yield the individual binary star masses ($M_1 = 0.9 \pm 0.3 M_\odot$ and $M_2 = 0.5 \pm 0.1 M_\odot$), semi-major axis (2.5 ± 1 AU), orbital period (3.1 ± 1.3 years) and distance from us (6.7 ± 0.3 kpc, *i.e.* in the Galactic bulge).

Shin et al. (2012a) analyzed eight binary-lensing events observed during seasons 2007-10 and determined their model parameters, but the degeneracy between close and wide binary models could not be broken for these events. Two other binary-star events were later reported, this time with their masses measured (Shin et al. 2012b): MOA 2011-BLG-090 ($0.43 M_\odot$ and $0.39 M_\odot$) and OGLE 2011-BLG-0417 ($0.57 M_\odot$ and $0.17 M_\odot$). Three of the stars involved in these two systems are M dwarfs. These stars are difficult to detect with other techniques, and these detections show that microlensing will be playing a more and more important role in helping constrain the fraction of binary stars as a function of mass.

Finally, the discovery of a very low-mass binary star in event OGLE 2005-BLG-153 was reported by Hwang et al. (2010). The masses of the two components were precisely measured ($M_1 = 0.10 \pm 0.01 M_\odot$ and $M_2 = 0.09 \pm 0.01 M_\odot$), just above the hydrogen-burning limit (*i.e.* $\sim 0.08 M_\odot$ or $\sim 80 M_J$). Such very low-mass binaries provide unique opportunities to better understand the demography of stars at the bottom of the Main Sequence, and subsequent formation process. Microlensing is of great help here because it does not rely on the brightness

of these objects, which are notably faint.

Exotic microlensing events

A number of microlensing light curves reveal exotic events. For example, in high-magnification event OGLE 2007-BLG-514 ($A > 1000$), Miyake et al. (2012) found that the light curve is most likely explained by a binary system in which the more massive component could be a white dwarf, a neutron star, or a black hole ($M_1 = 0.9^{+4.6}_{-0.3} M_\odot$, $M_2 = 0.2^{+1.2}_{-0.1} M_\odot$). Variable stars can also mimic microlensing events: for example, MOA 2010-BLG-523 has been identified as a special RS CVn variable star (Gould et al. 2013), the first of its kind to be spectroscopically confirmed in the Galactic bulge.

3. Detection of brown dwarfs

Brown dwarfs are failed stars, that are not massive enough to sustain hydrogen fusion. The first detection of a *bona fide* brown dwarf was the companion of the nearby star Gl229 (Nakajima et al. 1995), for which strong methane absorption confirmed it was too cool to be a star (Oppenheimer et al. 1995). At the same time, the first free-floating brown dwarfs were found in the Pleiades open cluster (by the detection of lithium absorption lines in their spectra, Rebolo et al. 1995). It is interesting to note that the first brown dwarf detections came in the same year as the discovery of the first extrasolar planet around a solar type star (Mayor & Queloz 1995).

An overlapping mass domain between brown dwarfs and planets

Traditionally, brown dwarfs are defined as compact gaseous objects with masses greater than $13 M_J$, which are massive enough to burn deuterium (*via* thermonuclear reaction $p+d \rightarrow \gamma+3He$, e.g. Chabrier et al. 2000) but cannot ignite hydrogen burning in their inner cores (around $74 M_J$, e.g. Burrows et al. 2001). This definition has led to a (somewhat arbitrary) classification of substellar objects : brown dwarfs occupy the mass range $13 - 74 M_J$, gaseous giant planets the range $100 M_\oplus$ (Saturn) – $13 M_J$, icy giant planets lie within $10 - 20 M_\oplus$ (Uranus and Neptune), super-Earth planets have $1 - 10 M_\oplus$ (these planets can be either terrestrial or partially gaseous), and terrestrial planets have masses equal or below an Earth’s mass (Earth, Venus, Mars and Mercury).

Isolated brown dwarfs are considered to form the tail of the very low-mass end of star formation processes, which proceeds by fragmentation and gravitational collapse of locally over dense cores inside turbulent molecular clouds (e.g. Hennebelle & Chabrier 2008). This is supported by observations of low mass stars and isolated brown dwarfs in young clusters such as σ Orionis, that indicate a continuous mass function down to masses as low as $\sim 6 M_J$ (Caballero et al. 2007). Several detections of medium-sized brown dwarfs surrounded by disks of material, as for stars, also support that picture (Luhman et al. 2005). The question, however, is more complex for *companion* brown dwarfs to stars. In fact, observation of a growing number of super-Jupiters (planets with mass

greater than $1 M_J$) have shown with no ambiguity that the observed frequencies of objects in the mass range $1 - 25 M_J$ behaves smoothly and presents no special feature at any mass, including at the deuterium burning limit of $13 M_J$. If this mass really did mark the transition between two distinct formation scenarios (for planets and brown dwarfs), a clear break in the slope of the mass function would be expected — but this is not observed. Hence, the generality of the previous definition of what a brown dwarf is, *i.e.* independent of the actual formation scenario, is now called into question. An alternative definition has been proposed, based on the formation mechanism rather than on a critical mass limit (e.g. Burrows et al. 2001). However, no clear consensus has emerged yet, though.

In proto-stellar (or proto-planetary) disks, two distinct paradigms for forming giant planets and objects more massive than $13 M_J$ are invoked: one is the *disk instability model* (or *direct collapse model*), for which direct gravitational instabilities in the proto-stellar disk directly build up the planet; the other theory is the *core accretion model*, in which a core is first built up by accretion of planetesimals that were made out of the fraction of solid material in the disk, and which eventually become heavy enough to accrete large amounts of gas from the disk. The gravitational instability scenario tends to favor the formation of massive giant planets in relatively large orbits (Boss 2006), but super-Jupiters of masses up to $38 M_J$ have been also successfully formed in recent simulations of the core accretion model (Mordasini et al. 2009). Hence, it is likely that the two processes overlap in strength in some range of masses between $\sim 5 - 74 M_J$. In some cases, Leconte et al. (2010) argue that the imprint of the formation process could be revealed by the size of the object’s radius, which is measured for transiting objects: a significant amount of heavy material would produce a smaller radius than that predicted for a brown dwarf formed by gravitational collapse (Baraffe et al. 2008), hence strongly advocating for a core accretion process. Only a few very close-in objects have been probed in this way however, and no definitive conclusions have yet been drawn from very inflated objects.

Brown dwarfs are commonly found as free-floating objects, but in spite of more than two decades of observations (mainly by radial velocity surveys), a paucity of companion brown dwarfs to stars have been established, while planets are frequent (Marcy & Butler 2000). For example, Sahlmann et al. (2011) derived an upper limit of 0.6% for the frequency of close-in brown dwarfs companions to FGKM Main Sequence stars. This paucity has been referred to as a “brown dwarf desert”, which currently holds for masses between $\sim 30 - 55 M_J$ and orbit sizes smaller than 3 AU, mainly for G-type primaries. An interpretation of this gap in the abundance of objects would be a transition regime between the largest objects that can be formed in a proto-planetary disk and the lightest objects that can be formed by direct collapse in the vicinity of a proto-star. But other authors such as Guillot et al. (2012) argue that the “desert” would simply be explained by a loss of an initial population of close-in massive giant planets and brown dwarfs due to tidal interactions: in this scenario, close-in, massive objects loose angular momentum due to the slower rotation of the star relative to the planet’s orbital motion, spiral in and fall into the star. This interpretation is supported by the discoveries of close-in brown dwarfs around F-type stars and the fact that this effect is predicted to peak for G-dwarf primaries.

Thus, the question of whether massive objects detected as companions to stars are formed by core accretion or gravitational collapse in the star’s proto-stellar disk, or by direct fragmentation and collapse in a clump close to the proto-star, is far from being resolved. Answers will come from the analysis of a significantly higher number of systems, including some detected with microlensing.

Detection of brown dwarfs through microlensing

Mao & Paczynski (1991) foresaw before any microlensing was observed that this method had a unique potential to discover brown dwarfs, and perhaps exoplanets (indeed, massive objects are easier to detect than lighter ones) — but planets were finally discovered long before the first brown dwarf. This is now understood as being due to a paucity of brown dwarf companions to stars. Compared to other techniques, microlensing opens a complementary window focused on M-dwarf hosts and brown dwarfs at large separations (detection at 10 AU and more). Historically, microlensing observations were focused on planetary events: other cases were usually not monitored as densely. In the last two decades, however, the pictures has dramatically changed with a steady progress in observational capabilities. With almost ten times more targets monitored today, an improvement of a factor of around hundred in the detection rate has been reached. As a result, many more binary events were detected, including several brown dwarf candidates.

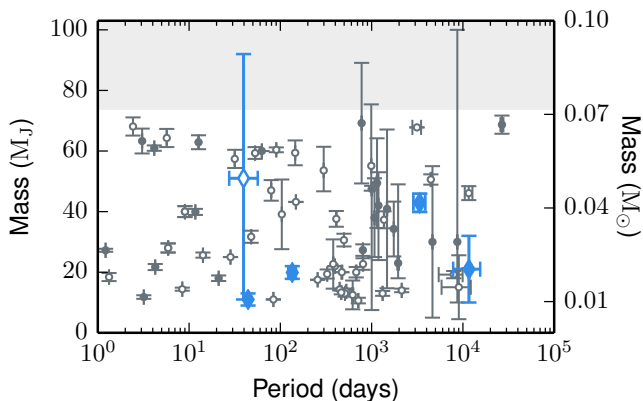


Figure 13: Microlensing (blue diamonds) and radial velocity (black circles) detections of brown dwarf companions to stars. The gray shaded region mark the stellar regime (figure from Ranc et al., in prep.).

Gould et al. (2009) reported the discovery of a *thick-disk isolated brown dwarf* at a distance of $D_L = 525 \pm 40$ pc, OGLE 2007-BLG-224 (thanks to terrestrial parallax effects). With a mass estimate of $M = 0.056 \pm 0.004 M_\odot$, it was the least massive thick-disk brown dwarf ever detected at this time. Further information on this object will be obtained in a few years when the lens and source are individually resolved. This detection at low detection efficiency suggests that old, substellar objects may be more frequent than usually assumed.

Discoveries of *brown dwarf companions to stars* are shown in Fig. 13, for microlensing and radial velocity data (List of RV data from Ma & Ge 2014). Shin et al. (2012c) analyzed binary events from seasons 2004-11 and extracted seven brown dwarf candidates, using the selection criterion $q < 0.2$ on the mass-ratio. These candidates were OGLE 2004-BLG-035, OGLE 2004-BLG-039, OGLE 2007-BLG-006, OGLE 2007-BLG-399 / MOA 2007-BLG-334, MOA 2011-

BLG-104/OGLE 2011-BLG-0172, MOA 2011-BLG-149, and MOA 201-BLG-278 / OGLE 2011-BLG-012. Two events were confirmed to be brown dwarfs: MOA 2011-BLG-104 / OGLE 2011-BLG-0172 with $M = 0.02 \pm 0.01 M_{\odot}$ and MOA 2011-BLG-149 with $M = 0.019 \pm 0.002 M_{\odot}$. In event MOA 2009-BLG-411L, Bachelet et al. (2012) found a brown dwarf of mass $M = 0.05 M_{\odot}$ orbiting a primary M dwarf of $M_{\star} = 0.18 M_{\odot}$. This discovery demonstrates that brown dwarfs exist in the vicinity of M dwarfs. Most likely, the two objects were formed by fragmentation and collapse of nearby gas clumps. Street et al. (2013) reported the detection of MOA 2010-BLG-073L, which also involved an M-dwarf primary ($M_{\star} = 0.16 \pm 0.03 M_{\odot}$), with a substellar companion ($M = 11 \pm 2 M_J$) at the limit of the brown dwarf regime ($13 M_J$). Bozza et al. (2012) reported the discovery of OGLE 2008-BLG-510, a potential event with a brown dwarf secondary, although the signature was too weak to unambiguously distinguish it from a binary star scenario. A brown dwarf companion with precise mass determination has been detected in event MOA 2007-BLG-197 (Ranc et al., in prep.).

Very tight, low-mass *brown dwarf binaries* have been detected by microlensing according to Choi et al. (2013): OGLE 2009-BLG-151 / MOA 2009-BLG-232 and OGLE 2011-BLG-0420, respectively with total masses of $0.025 M_{\odot}$ and $0.034 M_{\odot}$ and projected orbital separations of 0.31 AU and 0.19 AU. Both have relatively large mass ratios of $q \sim 0.4$, suggesting a gravitational collapse formation process. Such detections provide a unique incursion towards the lower-end tip of the brown dwarf mass function, showing that such binaries can form at least down to $0.02 M_{\odot}$.

Finally, a *planetary-mass object* of $1.9 \pm 0.2 M_J$ orbiting a *field brown dwarf* of $0.022 M_{\odot}$ at a distance of ~ 0.87 AU has recently been reported by Han et al. (2013) in event OGLE 2012-BLG-0358. The very small mass ratio of $q \simeq 8 \times 10^{-2}$ suggests that the companion has formed by core accretion in the proto-planetary disk surrounding the brown dwarf.

III. Detection and statistics of extrasolar planets

The *Solar nebula theory*, which explains the formation of the Solar system planets in a gaseous flattened disk in differential rotation, was proposed by Kant and later Laplace more than two hundred years ago. Planets were considered by a number of authors as by-products of a global process of star formation. The plurality of worlds was then a natural consequence of the plurality of stars. The hypothesis of planet formation in a disk of gas and dust was first supported by observations of envelopes of dust surrounding stars, betrayed by a flux excess in IR and UV. Direct detection of extrasolar planets has always been a great observational challenge, because the star-planet angular separation is extremely small, and the brightness contrast extremely high. Hence, only very recently have planets been detected by direct imaging. At the beginning of the 1990s, the only example of a planetary system was our Solar system.

The first exoplanets have been discovered by indirect methods. In 1992, the timing of the millisecond pulsar PSR1257+12 led to the discovery of planetary-

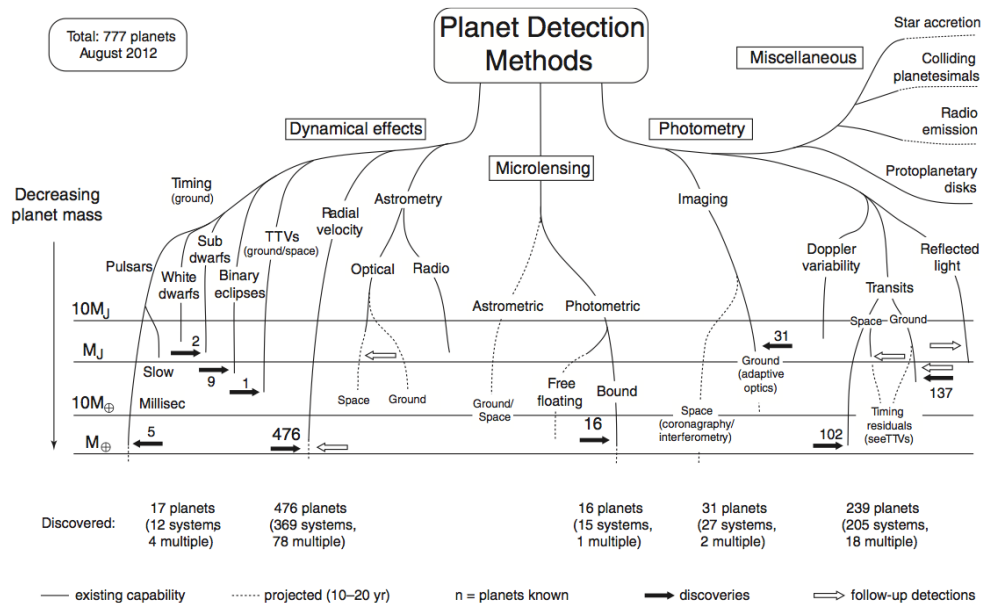


Figure 14: Schematic diagram of exoplanet detection methods, with status of discoveries as of August 2012. Many more detections have been since reported since (figure from Perryman 2012).

mass objects around this neutron star (Wolszczan & Frail 1992). A few years later, the first exoplanet orbiting a Sun-like star, 51 Peg (Mayor & Queloz 1995) was discovered by high-accuracy radial velocity measurements of the star’s periodic motion. These two landmark discoveries have initiated a novel, very active field in astrophysics: the search and characterization of extrasolar planets (see Fig. 14 for an overview of detection methods). At the end of 2013, the symbolic 1000th entry in the exoplanet catalogue was reached. Fig. 18 shows the incredibly rich variety of properties of the detected exoplanets. Microlensing caught its first exoplanet in 2003. Since then, detections have been made at an increasing rate, with many candidates currently being analyzed.

A. 2003-2005: microlensing milestone discoveries

1. The first exoplanet detected through microlensing

In 2003, the first microlensing planet discovery was reported by Bond et al. (2004) in event OGLE 2003-BLG-235/MOA 2003-BLG-53. This detection ended the (short) series of false detections made between 1999 and 2001 (Sahu et al. 2001; Rhie et al. 2000; Yock et al. 2000; Bennett et al. 1999). The light curve of OGLE 2003-BLG-235/MOA 2003-BLG-53 is shown in Fig. 15. The global shape of the light curve is typical of a single-lens event, but is affected by a short-duration, caustic-crossing deviation around $t = 2840$ (July 14–21, 2003), observed both in MOA and OGLE data. This event displayed an unusual short-duration (7 days), low-amplitude anomaly, a strong indicator of planetary events. The analysis of

the event light curve concluded that it was best explained by a binary-lens model with a mass ratio of $q = 0.0039^{+11}_{-07}$. The planet was then estimated to have a mass of $1.5 M_J$, and a semi-major axis of ~ 3 AU. An uncertainty remained, however, about the exact properties of the host star. To withdraw this ambiguity, Hubble Space Telescope data were collected by Bennett et al. (2006) two years later, after the lens and source were enough separated. The improved parameters determination yielded a slightly more massive planet of $2.6^{+0.8}_{-0.6} M_J$ at $4.3^{+2.5}_{-0.8}$ AU, and a host mass of $0.63^{+0.07}_{-0.09} M_\odot$.

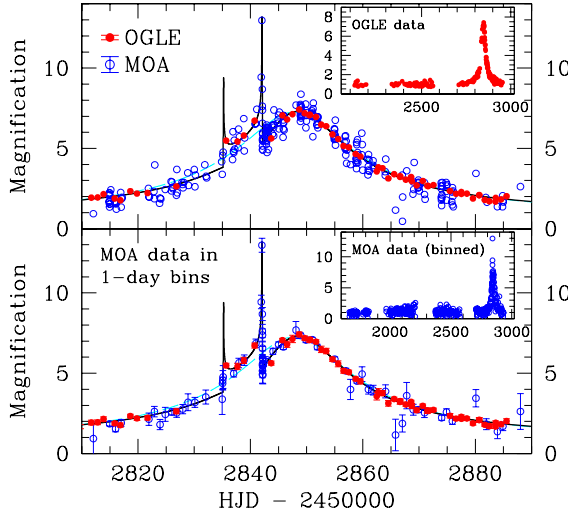


Figure 15: Light curve of the first exoplanet detected by microlensing, OGLE 2003-BLG-235/MOA 2003-BLG-53Lb, a Jupiter-like planet (figure from Bond et al. 2004).

2. First cool super-Earth: OGLE 2005-BLG-390Lb

On 11 July 2005, the OGLE Early Warning System (EWS) alerted OGLE 2005-BLG-390 (Fig. 16). The event was added on July 25 as a regular microlensing event into the PLANET follow-up list. The event peaked at a rather low magnification of $A_0 = 3$ on 31 July. Ten days later, on August 10, while the source was close to exit the Einstein ring, a deviation of 0.06 mag was noticed by observers at the Danish 1.54m telescope at La Silla. The anomaly was confirmed soon after by a new deviating point 0.12 mag above the single-lens model, later confirmed by OGLE. PLANET then triggered an internal alert: the PLANET Perth telescope started an automated continuous follow-up, while the PLANET telescope in South Africa was clouded out. The PLANET Danish telescope at La Silla (Chile) and Perth gathered six more data points, and combined with two additional measurements from MOA, the evidence of a planetary deviation was confirmed. An intense real-time modeling effort then started. The mass ratio was quickly found to be very small, $q \simeq 7.6 \times 10^{-5}$, possibly indicating a very low-mass planet. With a mass of $5.5 M_\oplus$ and semi-major axis of 2.6 AU, OGLE 2005-BLG-390Lb was the first cool super-Earth ever detected at large orbital separation (Beaulieu et al. 2006). The host star was an M dwarf of $0.22 M_\odot$ located in the Galactic bulge, at 6.6 kpc. While the planet should most likely be frozen,

for billions of years it may have preserved an ocean of liquid water underneath a protecting shell of ice, before it eventually completely froze (Ehrenreich & Cassan 2007; Marboeuf et al. 2008).

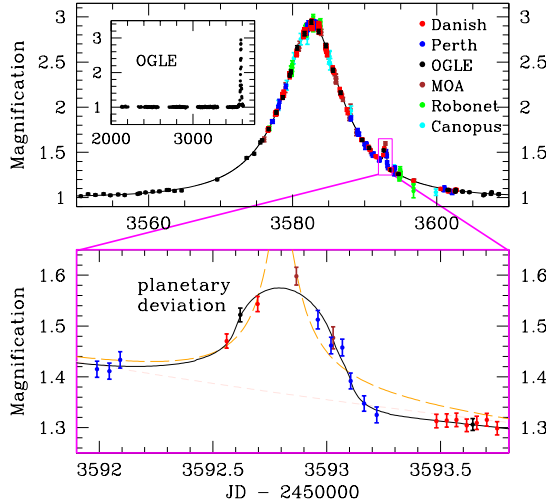


Figure 16: Microlensing light curve of the first cool super-Earth OGLE 2005-BLG-390Lb. The solid curve shows the best planetary model, involving a $5.5 M_{\oplus}$ planet at 2.6 AU from its host star. The dashed gray curve and the dashed orange line are respectively the best binary source and single lens models, that are rejected by the data (figure from Beaulieu et al. 2006).

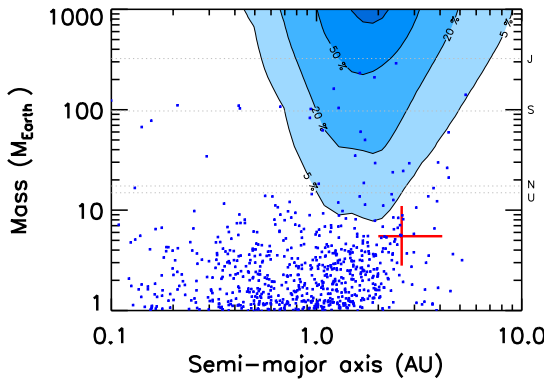


Figure 17: Blue contours draw the detection efficiency of an hypothetical, unseen second planetary companion to OGLE 2005-BLG-390Lb, as function of mass and semi-major axis. Blue dots represent the predicted final simulated distribution of a seed of 20000 planetary cores (Fig. 9 of Ida & Lin 2005) around an M dwarf of $0.2 M_{\odot}$ (figure from Kubas et al. 2008).

This discovery, made at low detection efficiency, suggested that a large population of low-mass planets may exist at large orbital distances, a prediction later confirmed by detailed statistical studies (Cassan et al. 2012). On the planet formation theory side, simulations by Ida & Lin (2005) or Laughlin et al. (2004) suggested that the formation of giant planets around (low-mass) M dwarfs would be largely inhibited, while super-Earths or Neptunes should be formed more easily. In order to test this prediction for OGLE 2005-BLG-390, Kubas et al. (2008) evaluated the probability of detecting an additional giant planet around the lens (related triple-lens geometry is shown in Fig. 8, p.16): in Fig. 17, blue contours label the computed detection probability as a function of mass and orbit size, while blue dots show the corresponding simulated population of planets by Ida & Lin (2005). The figure shows that massive planets would have been detected with high probability, which is compatible with most synthetic planets clustered

at low masses. A few weeks after the discovery of OGLE 2005-BLG-390Lb, a new super-Earth of $13 M_{\oplus}$ detected by microlensing was announced by μ FUN, OGLE 2005-BLG-169Lb (Gould et al. 2006), supporting further the idea of a higher frequency of low-mass planets compared to giant ones.

B. Microlensing planet discoveries

1. A panorama of detections

Fig. 18 shows the population of microlensing planets (until end of 2013, red dots) in the mass vs. semi-major axis diagram, together with the discoveries made with other techniques. The red and orange solid lines mark the approximate sensitivity domain of microlensing using ground-based telescopes. The sensitivity peaks at orbital distances of ~ 2 AU for M dwarfs and covers all masses down to that of the Earth.

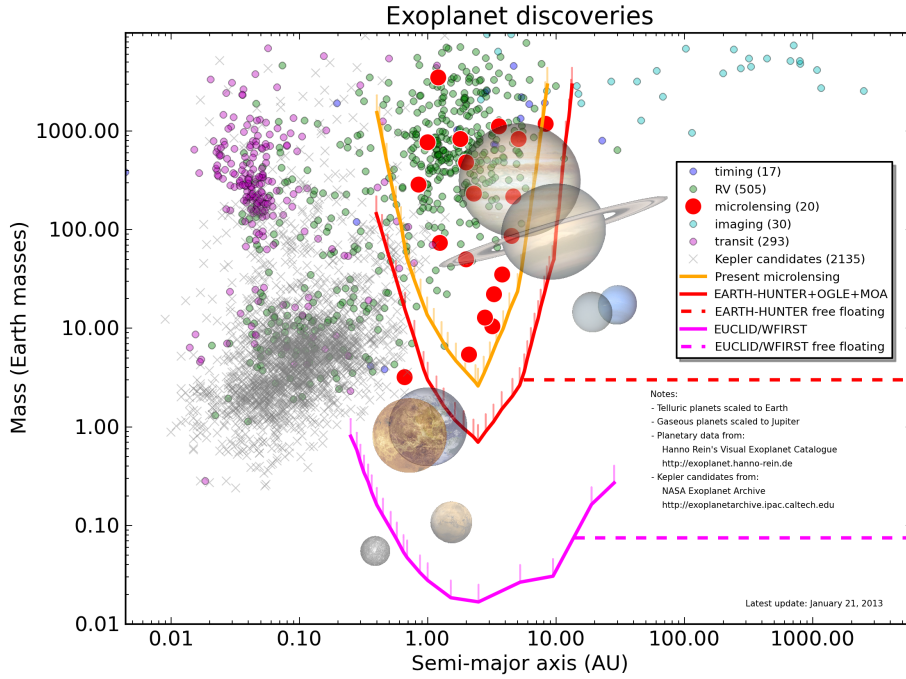


Figure 18: Planet discoveries as a function of mass and semi-major axis. Microlensing planets are marked in bold red. Red and orange solid lines mark the approximate sensitivity domain of ground-based microlensing surveys, while the pink line shows the expected sensitivity using a space-based microlensing observatory (figure courtesy J-B. Marquette).

An important information is whether the planet orbits within or without its star's snow line. The snow line (or ice line) is the distance to the star below which the temperature is low enough to allow ices to condensate in the proto-planetary disk. Solid cores of giant planets are thought to be formed beyond this line,

where sticking is more efficient and solid material more abundant. The location of the snow line approximately scales as (Kennedy & Kenyon 2008)

$$a_{\text{snow}} \simeq 2.7 \left(\frac{M_{\star}}{M_{\odot}} \right) \text{ AU}, \quad (32)$$

i.e., the more massive the star, the farther the snow line. Hence, microlensing sensitivity peaks at about three times the location of the snow line, and in fact, most microlensing planets are found to be outside the snow line, as seen in Fig. 19. For example OGLE 2011-BLG-0251Lb (Kains et al. 2013), a planet of $0.53 \pm 0.21 M_{\text{J}}$ orbiting a $0.26 \pm 0.11 M_{\odot}$ M dwarf star, lies at a projected orbital distance of $\sim 2\text{--}3$ AU, while the snow line lies at only 0.7 AU.

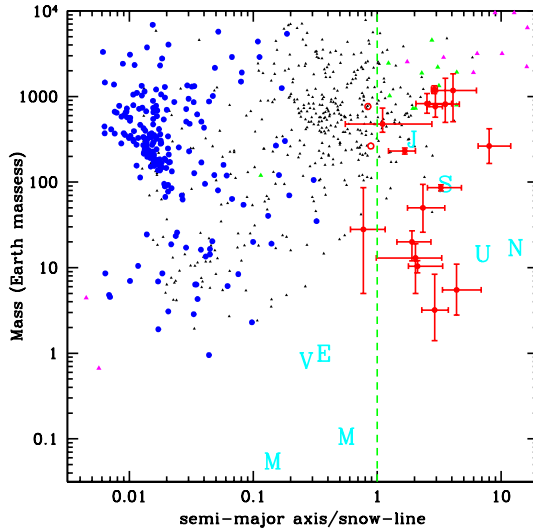


Figure 19: Planet discoveries as a function of mass and orbit, scaled to the location of the snow line. Microlensing planets are marked in red. Most of them are located beyond the snow line of their host star (figure from Mao 2012).

Besides planets, moons around massive exoplanets can be detected thorough microlensing (e.g. Liebig & Wambsganss 2010), although no firm detection has been made yet (Bennett et al. 2014).

Members of three remarkable populations of exoplanets have been discovered by microlensing: cool super-Earths, massive planets around low-mass stars, and free-floating planets. They are described below.

2. Cool super-Earths and Neptune-like planets

Low-mass stars (M and K dwarfs) form the bulk of microlensing planetary host stars. Around these stars, the core accretion scenario of planet formation predicts that Neptune-mass planets and super-Earths should be common (e.g. Laughlin et al. 2004). In fact, according to the core accretion scenario, a natural way to build up a giant planet proceeds as follows: when a core of solid material (rock and ice) has reached by accretion a critical amount of $5 - 15 M_{\oplus}$, a runaway process of gas capture starts and it becomes a giant planet, before the disk disperses (in about $2 - 10$ Myrs). But for low-mass disks and consequently low-mass stars, two facts can preclude the formation of giant planets. Firstly, the gas content of the

disk is less, and secondly, the dynamical timescales are longer for less massive stars, which imply that the gas may disperse before the planet has captured enough gas. It results that many failed-giants and low-mass planets should exist around low-mass stars, while very few giants should be observed. This prediction has been confirmed by microlensing observations: after OGLE 2005-BLG-390Lb (super-Earth) and OGLE 2005-BLG-169Lb (Neptune-like) mentioned earlier, a number of super-Earths and Neptunes were discovered. These are furthermore located at several AUs from their stars, beyond the snow-line, and are thus cool, frozen exoplanets.

MOA 2007-BLG-192Lb (Bennett et al. 2008) is the lowest-mass exoplanet detected by microlensing, with $3.2 M_{\oplus}$. It is particularly interesting because it orbits a very low mass M dwarf of $0.084 \pm 0.014 M_{\odot}$ (Kubas et al. 2012). This detection demonstrates that rocky planets can form around stars at the bottom of the Main Sequence. For MOA 2009-BLG-266Lb (Muraki et al. 2011), precise parallax measurements obtained with *EPOXI* (Deep Impact spacecraft) led to the discovery of a $10.4 \pm 1.7 M_{\oplus}$ planet at an orbital distance of 3.2 AU around a $0.56 M_{\odot}$ star. It may well be the first member of the population of “failed” gas giant planets mentioned earlier.

3. Massive planets around late-type stars

Amongst the 20 microlensing planets published by August 2013, 18 have masses greater than that of Saturn ($95 M_{\oplus}$), with 10 with masses greater than that of Jupiter. The M-dwarf host star sample ($M \leq 0.5 M_{\odot}$) includes 14 planets, amongst which 6 have masses above $1 M_J$. Hence giant planets account for about half of the sample of planets around M dwarfs. While this is naturally explained by the fact that massive planets are much easier to detect than less massive ones, these detections still suggest that they are not uncommon. This challenges in some way the core accretion scenario, which predicts a paucity of giant planets around M dwarfs as explained before.

As a matter of fact, a substantial fraction of planets around low-mass stars consists of super-Jupiters, *i.e.* giant planets with masses greater than $1 M_J$, located beyond the snow line. These are: OGLE 2005-BLG-071Lb ($M_{\star} \simeq 0.46 M_{\odot}$, $M \simeq 3.8 M_J$ and $a \simeq 3.6$ AU, Dong et al. 2009; Udalski et al. 2005), MOA 2009-BLG-387Lb ($M_{\star} \simeq 0.19 M_{\odot}$, $M \simeq 2.6 M_J$ and $a \simeq 1.8$ AU, Batista et al. 2011), OGLE 2012-BLG-0406Lb ($M_{\star} \simeq 0.59 M_{\odot}$, $M \simeq 3.9 M_J$ and $a \simeq 3.9$ AU, Poleski et al. 2014), and MOA 2010-BLG-073Lb ($M_{\star} \simeq 0.16 M_{\odot}$, $M \simeq 11 M_J$ and $a \simeq 1.2$ AU, Street et al. 2013). A scaled version of the gas giant planets of the Solar system (Jupiter and Saturn) was found around an M dwarf in event OGLE 2007-BLG-109 (Gaudi et al. 2008), with two giant planets of $0.7 M_J$ et $0.3 M_J$ at respectively 2.3 AU and 4.5 AU. Hence, there is a growing evidence that super-Jupiters exist around very low-mass stars. Current microlensing surveys should detect many more of these objects and allow first statistical studies of their properties.

4. Free-floating planets

Several free-floating, low-mass objects have been reported in young star-forming regions using optical and near-infrared imaging (e.g. Quanz et al. 2010; Zapatero Osorio et al. 2000). These objects extend from brown dwarf masses ($13 - 80 M_J$, where $M = 13 M_J$ is the deuterium burning limit at solar metallicity) down to the regime of massive giant planets (super-Jupiters, $M \geq 1 M_J$). A recent compilation of discoveries of planetary-mass objects together with L, T and very low-mass M dwarfs can be found in Liu et al. (2013).

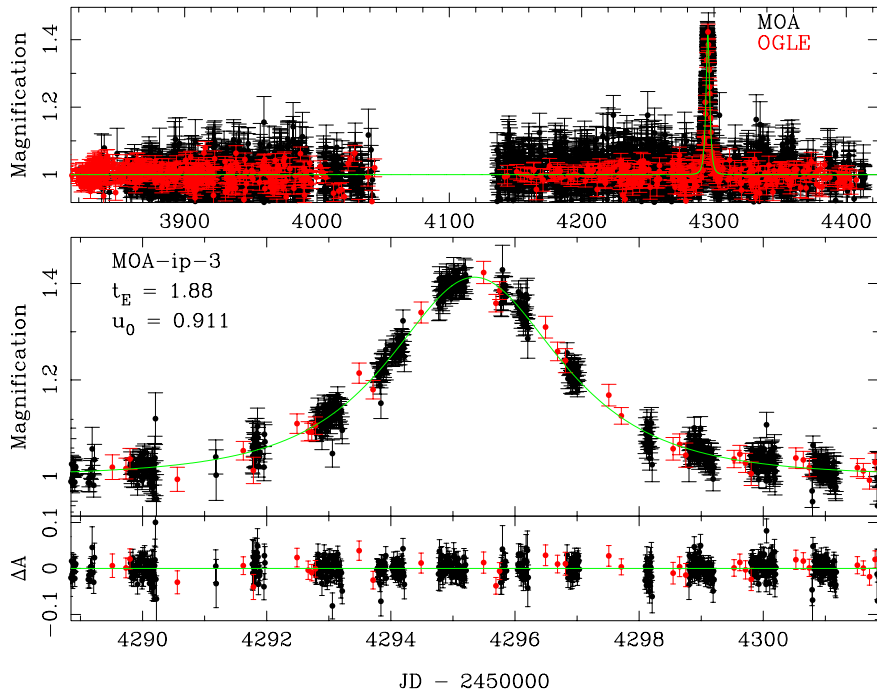


Figure 20: Light curve of MOA-ip-3, one of the ten very short duration microlensing events ($t_E < 2$ days) monitored by OGLE (red data points with error bars) and MOA collaborations (black data). The green line is the best-fit single-lens model. The upper panel shows the full two-year light curve, the middle panel is a close-up of the peak, and the bottom panel shows the residuals from the best-fit model in magnification units (figure from Sumi et al. 2011).

Free-floating, planetary-mass objects can be detected by microlensing as well. The typical duration of a microlensing event scales as $t_E \propto M^{1/2}$, so while stellar microlenses last several weeks to few months, isolated planetary-mass objects involve very short timescales of $t_E < 2$ days. The observational cadence required to detect and characterize such events is very high, but was already routinely achieved in 2006. In the MOA-II setup, 50 million stars in 22 bulge fields were continuously monitored. During the two seasons 2006-2007, MOA observed two central bulge fields every 10 minutes, and other bulge fields with a 50 minutes cadence, for a total of ~ 1200 microlensing events observed. Thanks to this high-

cadence strategy, several events with very short t_E were discovered. In the same period, OGLE-III observing cadence was 1-2 observations per night, but with higher quality photometry and a complementary coverage of the light curves. An example of the light curve of a free-floating object of Jupiter mass (MOA-ip-3) is shown in Fig. 20.

In 2001, Sumi et al. (2011) reported for the first time the discovery of several Jupiter-mass objects, free-floating or very distant from unseen host stars. They estimated their abundance as almost twice the number of main-sequence stars in the Galaxy. Statistical constraints from direct imaging furthermore suggested that a large proportion of them should be unbound to any star, *i.e.* free-floating (or “rogue”) planets. Hence, free-floating planets may be as common as stars in the Milky Way. While a formation by direct collapse of a cloud of gas and dust cannot be ruled out, it is likely that these planets formed in a proto-planetary disk, and were subsequently scattered into unbound or very distant orbits. In fact, dynamical instabilities in multiple planetary systems can explain extreme scenarios such as the ejection of a giant planet. A fraction of systems harboring giant planets with very eccentric orbits may be the last imprint of such a violent formation history.

C. *Statistical studies of Galactic populations of extrasolar planets*

1. 1995-2000: first upper limits on exoplanet frequency

Giant planets located at a few AUs, like Jupiter in the Solar System, were the prime targets of the first microlensing campaigns starting in 1995. The large caustic structures implied a planet detection efficiency as high as 100% on a well-covered event (Griest & Safizadeh 1998). Because of this very high detection efficiency, many giant planets should have been detected quickly. After a few and tens of events monitored, however, no planet was found yet. The cause of this negative result could of course have been an inadequate observing strategy — indeed it has since dramatically improved since —, but after a few years it became clear that giant planets were intrinsically rare. The hunt for extrasolar planets through microlensing revealed itself to be more challenging than initially thought.

To quantify the planet detection capabilities, Gaudi & Sackett (2000) proposed a quantitative method to compute microlensing detection efficiency, that we briefly summarize here. The planet detection efficiency $\varepsilon(\log d, \log q)$ is defined as the probability that a detectable planet signal would arise if the lens star has a companion with mass ratio q and separation d (more precisely, $\log q$ and $\log d$ since the size of the caustics are approximately power laws of d and q). A planetary signal is then defined as a $\Delta\chi^2$ exceeding a fixed threshold introduced by a planetary-lens model with parameters (d, q) relative to the best single-lens model that fits the data. This $\Delta\chi^2$ threshold is estimated *via* Monte Carlo simulations based on PLANET photometry of constant stars. $\varepsilon(\log d, \log q)$ is then obtained by varying the trajectory angle α within $[0, 2\pi]$ and by computing the fraction of angles for which $\Delta\chi^2(d, q, \alpha)$ exceeds the detection threshold.

Gaudi et al. (2002) used these principles to perform a statistical analysis of multi-site PLANET data gathered during the 5 seasons of observations 1995-99. The data sample was selected as follows: observed microlensing events were included in the analysis if they satisfied a number of criteria, such as a reasonable coverage of the light curve (e.g. more than 10 measurements), no evidence of any light curve anomaly, relative stability of the single-lens model parameters to less than 10%, homogeneous data sets with no obvious outliers, reasonable dispersion of the data. Final data sets were cleaned from obvious outliers and error bars were rescaled after a σ clipping. The first significant upper limits on the abundance of giant planets around red dwarfs were derived: less than 1/3 of the lens stars have Jupiter-mass companions, while less than 2/3 of the lenses have Saturn-mass companions in the orbital range 1.5 – 4 AU. Using a different method and data sets from OGLE only, Tsapras et al. (2003) analyzed three years of data (1998-2000) and found an upper limit of 20% on the abundance of Jupiter-mass planets. Snodgrass et al. (2004) later analyzed OGLE 2002 data, and derived an upper limit of 18% for Jupiters at 4 AU. All upper limits mentioned here are compatible with current estimates of the frequency of giant planets (around 17%, Cassan et al. 2012).

2. The 2005-08 high-magnification sample

The μ FUN collaboration (closely working with PLANET and other collaborations) took advantage of a growing community of amateur astronomers observing microlensing events (in particular in New Zealand) to set up a very reactive observing strategy dedicated to detect and characterize high-magnification events (the time window for detection decreases with increasing peak magnification). During the 4 seasons 2005-08, high-magnification events were monitored as intensively as possible, independent of any evidence of a light curve anomaly (“controlled experiment”): half of all high-magnification events could be correctly characterized. This strategy turned out to be very efficient: half of the events monitored turned out to be planetary events. In order to estimate the planet frequency from this high-magnification sample, an unbiased sample of 13 high-magnification events with peak magnification greater than 200 (gray cumulative histogram of Fig. 21) was selected by Gould et al. (2010b). They derived a planet frequency of $0.36 \pm 0.15 \text{ dex}^{-2}$ in $\log q \times \log d$ (translated in logarithms of mass and semi-major axis in Fig. 23). This result was consistent with Doppler estimates of Cumming et al. (2008), when considering that Doppler hosts are G dwarfs rather than M dwarfs, and when planetary systems are scaled to the location of their snow line. Gould et al. (2010b) finally estimated that 1/6 of all planetary systems would resemble our own Solar system.

In the study of Gould et al. (2010b), only the normalization of the planetary mass function around Saturn’s mass could be estimated. Sumi et al. (2010) argued that with 10 planet detections available in 2010, an estimate of the mass function slope could be obtained, assuming that in first approximation the detection efficiency follows $\varepsilon(d, q) \propto q^\alpha$ (regardless of the actual detection efficiency of the events). They derived a slope of -1.68 ± 0.2 , which is displayed as the blue

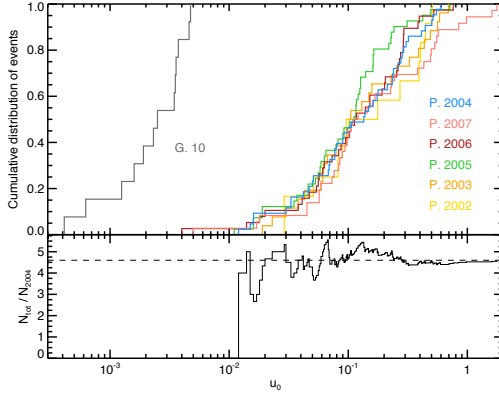


Figure 21: The upper panel shows the cumulative distributions of the impact parameter u_0 for microlensing events in the PLANET+OGLE 2002-07 sample (colored curved marked 'P', Cassan et al. 2012) and for the high-magnification sample ('G' gray curve, Gould et al. 2010b). High-magnification events have small u_0 and are seen on the left-hand side of the graph (figure from Cassan et al. 2012).

line in the right upper corner of Fig. 23. This result implied that Neptune-mass planets beyond the snow line of M dwarfs should be 7^{+6}_{-3} times more common than Jupiters.

3. PLANET+OGLE 2002-07: One or more planets per Milky Way star

Since 1995, the PLANET collaboration has been working as a network of telescopes following-up at high-cadence alerts from survey telescopes. With a database rich with about 15 years of data in 2010, it potentially had a much higher sensitivity to low-mass planets than that of Gaudi et al. (2002). Cassan et al. (2012) analyzed 1995-2010 PLANET data alerted by OGLE, using detections and non-detections.

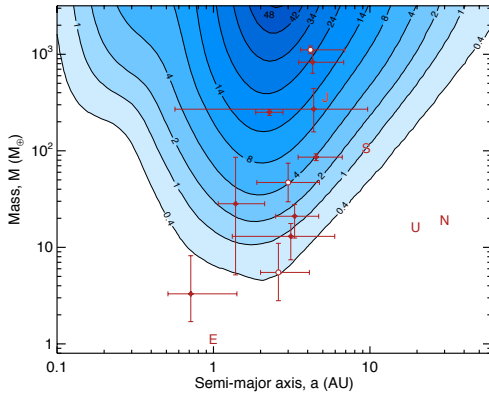


Figure 22: Blue contours indicate the expected number of detections from PLANET+OGLE 2002-07 data, if all lens stars have exactly one planet with orbit size a and mass M . The red open circles with error bars mark the planet detections included in the study (figure from Cassan et al. 2012).

In order to be combined in a meaningful statistical analysis, two critical conditions were required. First, the observing strategy should be well understood and keep homogeneous for the whole sample of events, which required that the event selection and sampling rate was chosen regardless of whether the lens harbored a planet or not. Secondly, the detections should result from exactly the same strategy than for the non-detections. It resulted from a detailed study of the statistical properties of the microlensing events that only a sub-sample of

six years of data, 2002-07, satisfied the given requirements. In fact, when starting its new operations in 2002, OGLE III dramatically increased its number of alerts compared to OGLE II (389 in 2002 vs. 78 alerts in 2000), which had a strong impact on the PLANET strategy. After 2007, a very open collaboration between the different microlensing teams again resulted in a dramatic change in the observing strategy. During 2002-07, PLANET monitored around 10-16% of all OGLE alerts.

In Fig. 21, the cumulative distributions of impact parameters for these six PLANET seasons appear remarkably homogeneous (colored curve with label 'P'). By comparison, the high-magnification sample of Gould et al. (2010b), in gray, has very different properties, as expected. Hence, although using the same microlensing technique, two independent studies resulting from two different observing strategies were conducted.

The planet sensitivity, based on non-detections, is shown in Fig. 22: blue contours mark the expected number of detections (in 2002-07) if all lens stars had exactly one planet with orbit size a and mass M . The detection sample included the three detections compatible with PLANET+OGLE strategy: OGLE 2005-BLG-071Lb, OGLE 2005-BLG-390Lb and OGLE 2007-BLG-349Lb (red open symbols with error bars).

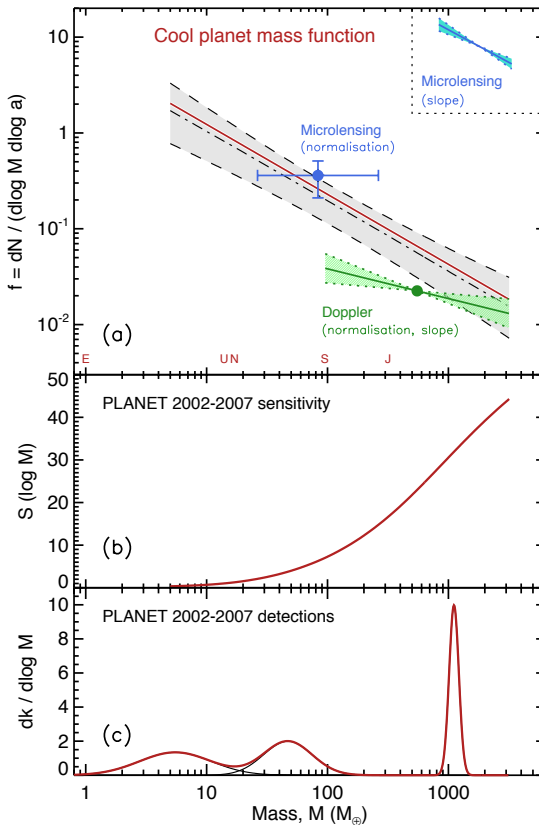


Figure 23: Planetary mass function as derived by microlensing and Doppler techniques (upper panel). Results from Gould et al. (2010b) and Sumi et al. (2010) are respectively the blue point with error bars (normalization) and the blue lines (mass function slope). The combined result including 2002-07 PLANET+OGLE data is shown as a red solid line with inside the 68% c.l. gray-shaded area (normalization, slope). Measurement from Cumming et al. (2008) Doppler survey is shown in green (normalization, slope). The middle panel shows PLANET 2002-07 sensitivity integrated over mass, while the lower panel displays the mass probability densities of the three detections included in the study (figure from Casan et al. 2012).

Fig. 22, clearly shows that the detection sensitivity ranges from $5 M_{\oplus}$ to $10 M_J$ and 0.5 to 10 AU, and the median mass of the host stars is in the M

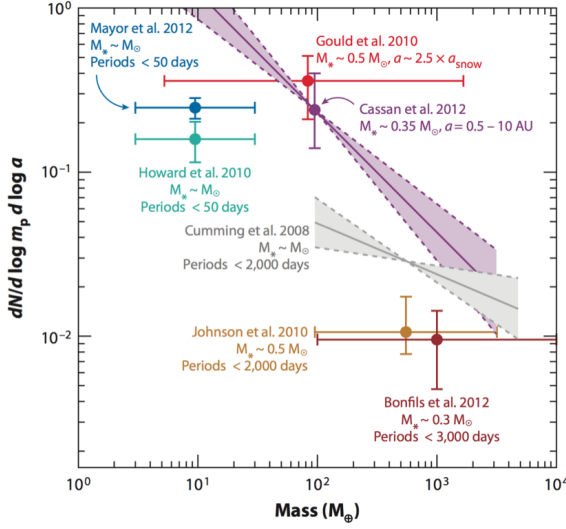


Figure 24: Various planetary mass function constraints from different analysis using microlensing and radial velocity data (figure from Gaudi 2012).

dwarf regime ($0.35 M_{\odot}$). Detections and non-detections were then combined in a Bayesian framework to constraint a power-law planetary mass function (no obvious dependance was found in a , following Öpik's law):

$$f(\log a, \log M) \equiv \frac{d^2 N}{d \log a d \log M} = f_0 \left(\frac{M}{M_0} \right)^{\alpha}, \quad (33)$$

where N is the average number of planets per lens star, f is the number of planets of mass M per decade of planet mass per decade of semi-major axis and per star, f_0 is the planet abundance (in $\text{dex}^{-2} \text{star}^{-1}$) at some pivot-point mass M_0 , α is the slope of the mass function with regard to M . A power-law seems here a natural choice because detections appear to span uniformly the mass range, as seen in Fig. 22. Constraints from Gould et al. (2010b) and Sumi et al. (2010) were added as Bayesian priors. Cassan et al. (2012) derived the following planetary mass function,

$$f = 10^{-0.62 \pm 0.22} \left(\frac{M}{95 M_{\oplus}} \right)^{-0.73 \pm 0.17}, \quad (34)$$

centered on Saturn's mass. It is presented in Fig. 23 as the red solid line with 68% confidence region (shaded). A recent compilation of microlensing and Doppler results is shown in Fig. 24 (Gaudi 2012). Cassan et al. (2012) finally estimated that $17^{+6}_{-9}\%$ (1/6) of stars host Jupiter-mass planets ($0.3\text{--}10 M_J$), while cool Neptunes ($10\text{--}30 M_{\oplus}$) and super-Earths ($5\text{--}10 M_{\oplus}$) are even more common, with respective abundances per star of $52^{+22}_{-29}\%$ (1/2) and $62^{+35}_{-37}\%$ (2/3). Hence, planets around Milky Way stars are the rule, rather than the exception, as illustrated in Fig. 25.

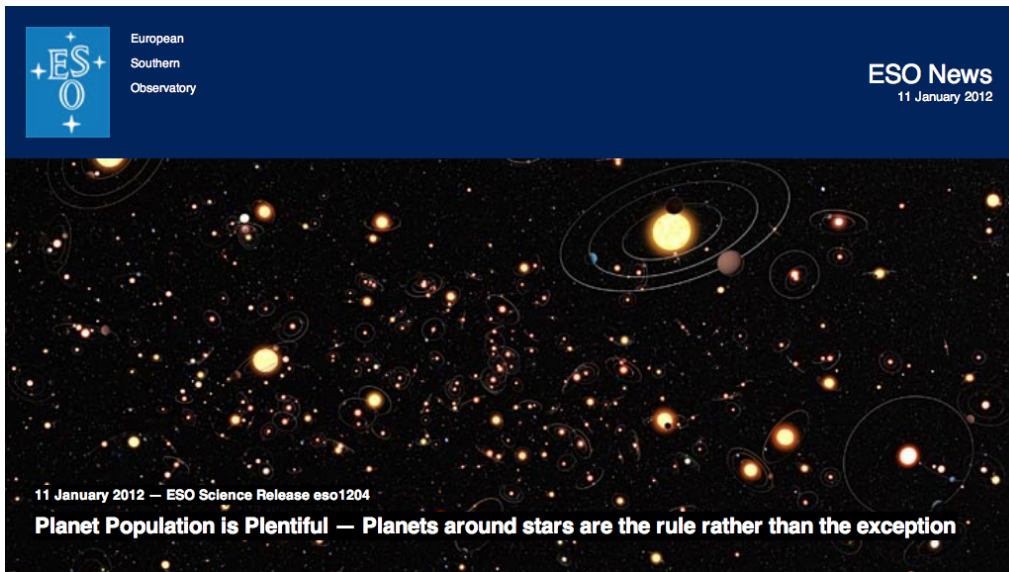


Figure 25: An artist’s impression illustrating that planets are as common as stars in the Milky Way: one in six stars host a Jupiter-like planet, half have Neptune-mass planets and two thirds host super-Earths (Artist’s impression from ESO News, Science Release eso1204. Image credit: ESO/M. Kornmesser).

IV. Towards a large scale microlensing planet search

A. A new generation of ground-based telescopes

1. Networks of robotic telescopes with wide-field cameras

The two historical microlensing surveys, OGLE and MOA, upgraded a few years ago their CCDs to wide-fields cameras. This technological improvement resulted not only in a greater number of events monitored, but changed profoundly the observational strategy. In fact, from classical operations using a survey telescope which alerted events that were followed-up by networks of narrow-field telescopes, the strategy is now evolving towards individual telescopes which can perform the two tasks: detection and follow-up. Nevertheless, networks of telescopes are still needed to ensure a 24h coverage of the light curves, and allow for redundancy between data sets. The projects mentioned below will benefit from a long history of collaboration, and from the contribution of many amateur astronomers using small but high-quality telescopes.

Since March 2010, OGLE-IV operates a telescope with a field of view of 1.4 square degrees. From 700 alerts issued in 2009, around 2000 events per season are now detected. MOA-II has been equipped with a new mirror of 1.8m and a new camera with a field of view of 2.2 square degrees. The RoboNET collaboration (Burgdorf et al. 2007; Horne et al. 2009; Dominik et al. 2007) has been operating robotic telescopes for about ten years, as part of PLANET operations. It integrated a few years ago the Las Cumbres Observatory Global Telescope network (LCOGT, e.g. Tsapras et al. 2009). Today the network already includes 2 robotic

telescopes of 2m, that should be complemented by 24 smaller telescopes of 40cm, partly dedicated to microlensing.

The Korean Microlensing Network (KMTNet, Poteet et al. 2012) is currently under construction, and should be fully operational in about 5 years. It consists in the deployment of a dedicated network of three 1.6m robotic telescopes located in Chile, South Africa, and Australia. Each telescope will be equipped with a 4 square degrees camera. KMTNet will perform a continuous survey of microlensing events through four fields at a cadence of 10 minutes, with 2 minutes for each field.

The Chinese Academy of Sciences has also proposed to build 2 telescopes of 2m class in Argentina and Antarctica (Dome A). The advantage of a telescope in Antarctica is that it can conduct a continuous survey of the Galactic bulge during the polar night. In practice, observations in such an extreme environment poses several technical issues. Nevertheless, a pilot survey including three 50 centimeter telescopes has been started at Dome-A early 2012.

As to the development of the PLANET network, it will soon operate in Australia the new robotic telescope of the University of Tasmania (historical PLANET partner): the Bisdee Tier Optical Astronomy Observatory. The telescope is robotic, has a diameter of 1.27m and is equipped with the former OGLE-II camera (0.5 square degrees).

2. Astrometry and interferometry

During a microlensing event, a number of images of the source are produced by the lens (Fig. 26). But as mentioned earlier, their separation is too small (around 0.5 mas) to be resolved by classical telescopes, and only the time-dependent magnification of the source flux has been exploited yet. Recent high resolution techniques, however, could allow a direct measurement of the separation of the images: astrometry and interferometry. Here we provide a short description of the perspectives associated with these two promising techniques.

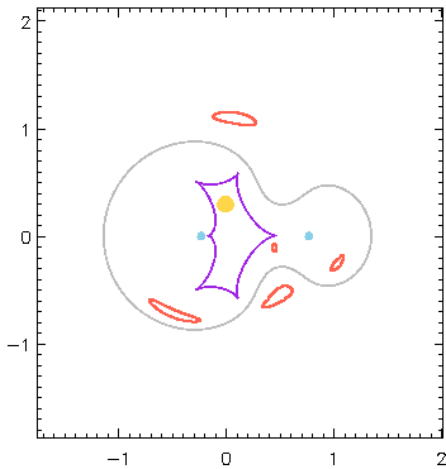


Figure 26: The image shows a binary lens with its two components (blue dots). The grey lines are the critical curves (lens plane) while the violet lines are the caustics (source plane). During a microlensing event, the source (yellow disk) is split into different images (red contours), that can in principle be resolved by current high-resolution techniques, such as astrometry and interferometry (figure produced by simulation code FORELENSER, A. Cassan).

Astrometric measurements rely on the fact that the *centroid* of all the images

moves during a microlensing event, while the different images themselves are not resolved. The amplitude of the centroid's trajectory is of order of the angular size of the Einstein's ring or a fraction of a mas (e.g. Cassan 2005). More precisely, the value of θ_E can be derived from the amplitude of the centroid's motion, which provides an independent relation between the microlensing parameters. The required astrometric precision is at reach of a space telescope like ESA's satellite GAIA (Belokurov & Evans 2002), and in fact the GAIA Alert group involves microlensing alerts. An interesting aspect of astrometric microlensing is that while the magnification behaves as

$$A \simeq 1 + \frac{1}{u^4} \quad (35)$$

with u , the lens-source distance in θ_E units, the images centroid shift behaves as

$$S \simeq \frac{\theta_E}{u}. \quad (36)$$

Hence, since u increases away from the peak, the *astrometric* microlensing event lasts much longer (duration $\propto 1/u$) than the *photometric* event (duration $\propto 1/u^4$).

Interferometric observations allow a direct measurement of the separation between the images (Rattenbury & Mao 2006; Delplancke et al. 2001). This is because they are exactly in the range of resolution (mas) currently achieved by long-base interferometers (100m), such as ESO Very Large Telescope (VLT) or CHARA (Center for High Angular Resolution Astronomy) in Mount Wilson. Two telescopes can be used for visibility measurements, but when more telescopes can be combined, phase closure (Dalal & Lane 2003) and imaging are possible. A simulation of an interferometric follow-up of a microlensing event is shown in Fig. 27. The difficulty of the observation resides in the fact that only the fraction of bright microlensing events can be monitored by an interferometer. They include bright sources or high-magnification events, and preliminary simulations show that today, 2 to 10 microlensing events could be monitored every year. The observational strategy would consist in selecting interferometric microlensing targets a few days in advance (which is relatively easy for high-magnification events), and in imaging the interferometric (u, v) plane for a few hours. Combined with the (photometric) light curve parameters, interferometry then provides an independent measurement of θ_E , as with astrometry.

B. Microlensing planet search from space

1. Advantages

Microlensing observations from space have two main advantages compared to ground-based monitoring (Bennett & Rhie 2002). Firstly, faint, main-sequence source stars can be routinely observed from space, while giant sources are preferred from the ground to secure high-precision photometry. Hence, an increase of an order of magnitude in the number of microlensing event alert should be expected. Secondly, observing main-sequence source stars strongly increases the

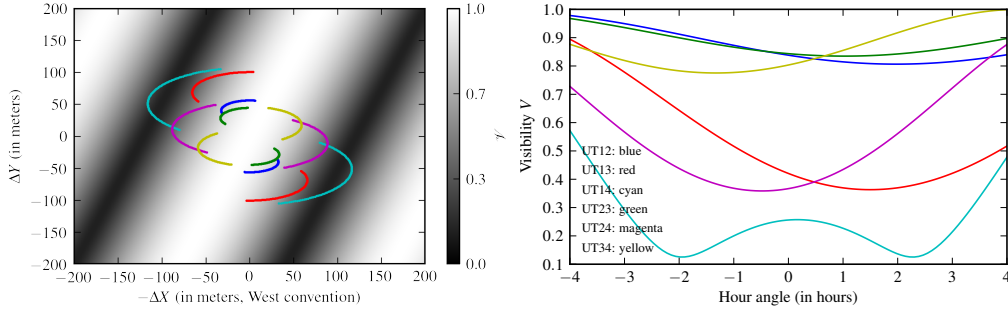


Figure 27: The left panel shows the coverage of the (u, v) plane of a microlensing event for all possible combinations of two telescopes amongst the 4 UTs of the VLT. The interferometric visibility (contrast) due to the multiple images is shown in grey scale. The right panel displays the corresponding visibilities as a function of time (figure from Ranc & Cassan, in prep.).

planet detection sensitivity, as illustrated in Fig. 28: the smaller the angular size of the source, the longer and more pronounced the planetary light curve anomalies (secondary peaks).

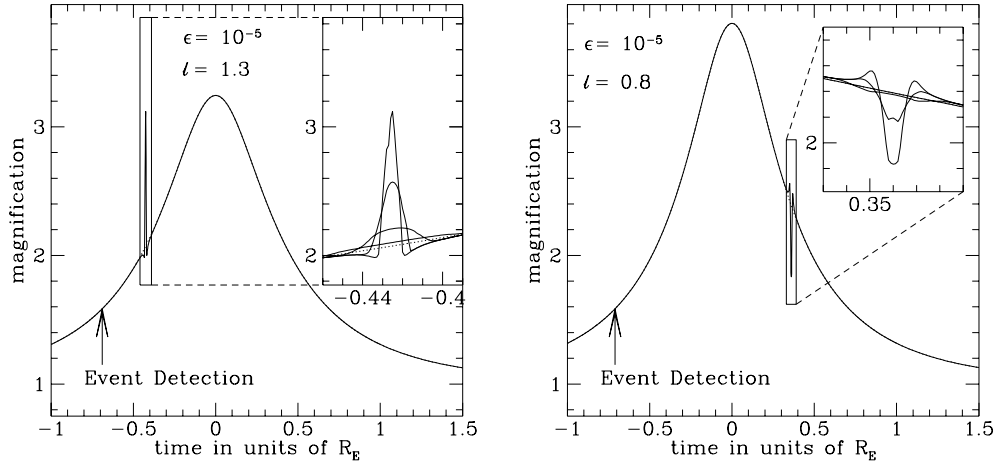


Figure 28: Simulated microlensing anomalies for two different lensing configurations, both for mass ratio $q = 10^{-5}$. On the left panel, the binary-lens separation is $d = 1.3$ (wide configuration), and on the right panel $d = 0.8$ (close configuration). The insets display the signal for different source radii in θ_E units: 0.006, 0.013 and 0.03, with the smallest radii leading to the sharpest and most peaked signals (figures from Bennett & Rhie 1996).

2. Planet yield estimation

Microlensing observations from space require a wide field of view ($\sim 0.5 \text{ deg}^2$), a small pixel scale, and a large collecting area to perform high-precision photometry of main-sequence Galactic bulge stars in relative short exposure times. It was

understood quickly that microlensing planet search and weak lensing surveys from space share very similar instrument requirements (Beaulieu et al. 2010; Gould 2009). The cost of a combined mission would be much less than that of two individual missions. In particular, the ESA Euclid³ spacecraft instruments would be well-suited for carrying out a deep microlensing planet search, as a legacy science program (Beaulieu et al. 2010).

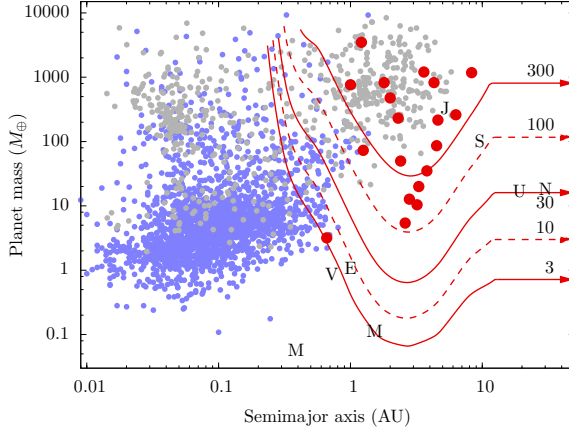


Figure 29: Planet yield for a 300-days survey (red lines), assuming that every lens star has one planet. Microlensing detections are in red, other planet detections or candidates are in gray and blue (figure from Penny et al. 2013).

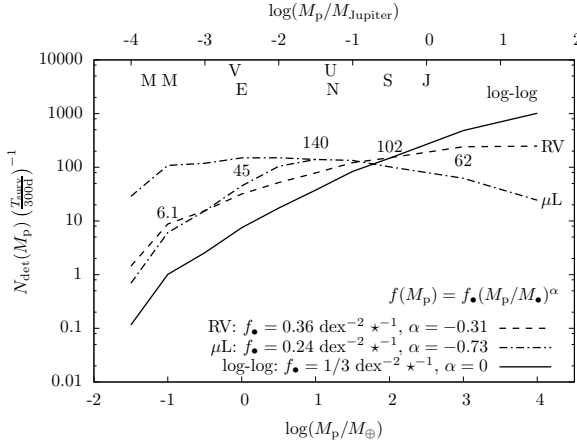


Figure 30: Planet yield estimates as a function of planet mass, for different planetary mass functions: "RV" (radial velocities+microlensing), " μ L" (microlensing alone) and a naive log-log mass function for reference (figure from Penny et al. 2013).

Euclid is an ESA Cosmic Vision M-class mission. The spacecraft will comprise a 1.2-m Korsch telescope with a high-resolution optical imager (VIS) and a near infrared imaging spectrometer (NISP). Penny et al. (2013) and the Euclid Exoplanet Science Working Group simulated a 5-years long, 300-days mission with two uninterrupted 30-day planet search seasons per year, 20-mins observing cadence with NISP (Kerins et al. 2009). A realization of the Besançon Galactic population synthesis model (Robin et al. 2003) was used for the first time to generate synthetic microlensing events. The survey would follow over 10^4 reasonably magnified microlensing events during the overall mission, an order of magnitude larger than can be achieved by current ground-based telescopes.

The survey sensitivity diagram is shown in Fig. 29. Each lens star in the simulation is assumed to host a single planet with semi-major axis 0.03-30 AU.

³or NASA WFIRST, a space mission recommended by the US Decadal Survey.

The red dots mark the current microlensing planet detections, and the red lines are labeled with the expected total planet yield. The survey is sensitive to planets with masses as low as Mars, and planets with orbits as large as 20 AU should be detectable. Fig. 30 shows the expected planet yield, for different mass functions, determined by radial velocities or microlensing (Cassan et al. 2012). Such a survey would perfectly complement the CoRoT and Kepler planet transit space missions, and provide a first census on planet populations for all orbits below 20 AU.

C. Advanced modeling

With the fast development of new telescopes and instruments, more than an order of magnitude of microlensing events are to be expected every year. But this large flow of data is currently out of reach of available modeling tools: only the most interesting fraction of all events can be studied in detail. In fact, the analysis of anomalous microlensing events light curves poses great computational challenges. Models can include second order effects, such as finite source or parallax, which dramatically increase the volume of the parameter space and model degeneracies. To handle this CPU-intensive task, advanced modeling tools are required. Ideally, light curve features should be automatically recognized, and suitable models with initial parameter guesses proposed. Bayesian algorithms optimized for microlensing models also have proven to provide a better interpretations of the data. Hence, a special effort has been paid recently to develop efficient, robust and automated modeling tools, as described below.

1. Numerical methods

The exploration of the full microlensing parameter space requires a large number of light curves to be computed. While single-lens models are straightforward to obtain, binary-lens and caustic crossing events usually poses great numerical challenges, even to compute a single model. Minimization schemes involve in particular parameter grid searches, genetic algorithms (Cassan 2005; Kubas 2005), simplex downhill and gradient methods, Markov Chain Monte Carlo (MCMC), and many other techniques when needed. When the source star approaches a caustic region, it cannot be considered anymore as point-like. The typical source-caustic distance at which finite source effects are no longer negligible is of order of three source radii (a little more when a cusp is involved).

Finite-source effects can be computed in different ways. Outside of caustic regions, a Taylor expansion up to the hexadecapole approximation of the total extended-source magnification can be relatively easily obtained (Gould 2008). The magnification is then computed by evaluating the point-source magnifications of 13 points at specific locations onto the source's disk. The calculation is an order of magnitude slower than point-source, but many orders of magnitude faster than a full integration. In caustic regions, this method breaks down (new images of the source created) and a full integration is required. While integrating the point-source magnification over the source star surface seems the most

straightforward solution, in practice it usually poses computational challenges because of the divergence of the magnification on the caustics. To avoid this problem, the integration can be performed in the *lens plane* along the contour of the images (Stokes theorem). The difficulty thus resides in determining efficiently the images shape (Gould & Gaucheron 1997). Adaptive contouring methods have been proposed to optimize the search of the image contours without solving the lens equation (Bozza 2010; Dominik 2007).

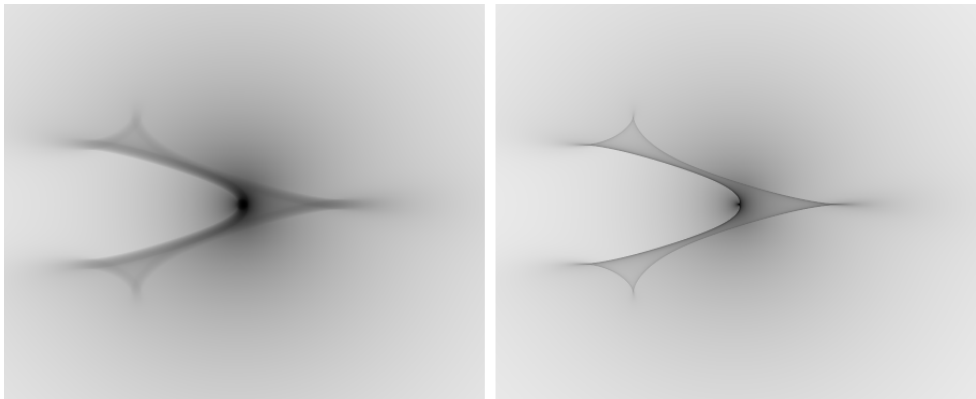


Figure 31: Two examples of ray-shooting magnification maps for an intermediate binary lens. The darker regions have highest magnification. The map on the right is computed for a point-source (in practice, a pixel), while the map on the left has been convolved with an extended source with a limb-darkening profile (figure from Cassan 2005).

Finite-source effects can also be computed with a completely different method: the ray tracing (or inverse ray shooting) technique. The lens plane is divided into a dense grid of points from which light rays are shot and end up in the source plane (*i.e.* travel backward). The density of rays collected in the source plane is then proportional to the magnification, and a full magnification map is drawn as shown in Fig. 31. These maps are very useful since they can be pre-computed and convolved with any kind of source shape and brightness profile. In particular it is well suited for statistical studies where a large number of events must be modeled (Cassan et al. 2012). The ray-tracing technique can also be used in real-time, but it requires to determine beforehand the position of the images. Finally, it has been demonstrated that Graphical Processors Units (GPU) can be used very efficiently to create ray-shooting maps, essentially because it is a parallel process.

2. Light curve features-based modeling

An automatic modeling software would rely primarily on algorithms that are able to recognize light curve features and help select adequate models, and speed up calculations by choosing the right approximations. The most common light curve anomalies are due to caustic crossings. Since binary lenses account for almost 10% of all microlensing events, including all planetary events, they require very special attention. Historically, the first event that exhibited caustic-crossing features was OGLE No. 7 (Udalski et al. 1994). The first microlensing planet also involved a

caustic anomaly (Bond et al. 2004). Albrow et al. (1999) proposed for the first time to specifically use caustic-crossing light curve features in the description of a binary-lens model. The technique was applied to event MACHO 98-SMC-1 (Afonso et al. 2000) and proved to be very efficient.

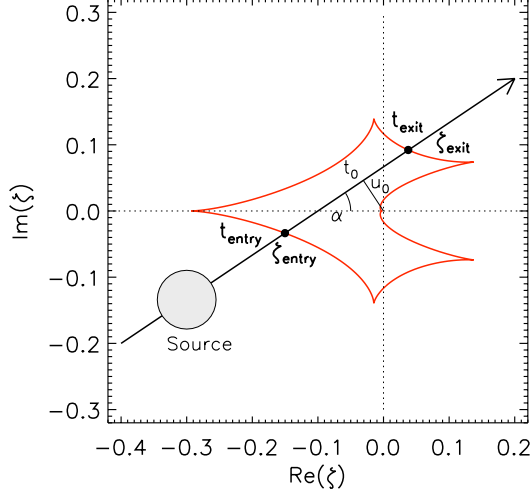


Figure 32: The $(t_{\text{in}}, \zeta_{\text{in}}, t_{\text{out}}, \zeta_{\text{out}})$ parameterization ("in" and "out" are labelled "entry" and "exit" in the figure) as compared to the more classical u_0, t_0, α, t_E , for a $(d = 1, q = 10^{-2})$ binary lens. Caustics are marked in red. The source trajectory (black arrow) crosses the caustic at curvilinear abscissa s_{in} and s_{out} , which correspond to points ζ_{in} and ζ_{out} on the caustic line (figure from Cassan 2008).

The caustic pattern of a static binary lens depends only on the separation d and mass ratio q of the two components. Classically, the source center trajectory is specified by the impact parameter u_0 relative to the origin, the trajectory angle α , the time at closest approach to the origin t_0 and the Einstein radius crossing time t_E . The corresponding parametrization is illustrated in Fig. 32. To take advantage of the observed dates of caustic entry and exit, Cassan (2008) introduced two alternative parameters t_{in} and t_{out} , and worked out a formalism to complete the model by additional parameters s_{in} and s_{out} , which are the abscissa along the caustic line of the ingress and egress points of the source center trajectory. The two-dimensional coordinates of the entry and exit are $\zeta_{\text{in}}(s_{\text{in}})$ and $\zeta_{\text{out}}(s_{\text{out}})$ in Fig. 32. These parameters make it much easier to locate all possible source-lens trajectories that fit the light curve, because they all produce caustic crossing features at the observed dates. The search of the parameter space is conducted by finding the pair $(s_{\text{in}}, s_{\text{out}})$ that best fits the light curve, with a simultaneous adjustment of the entry and exit dates $(t_{\text{in}}, t_{\text{out}})$. This parametrization is thus more general than that of Albrow et al. (1999). Furthermore, the source radius ρ can be estimated, and it provides a natural formalism to model rotating lenses (e.g. Penny et al. 2011; Jung et al. 2013).

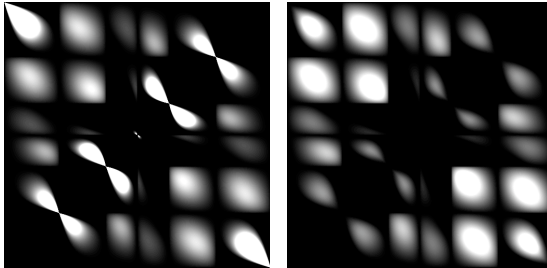


Figure 33: Examples of Bayesian priors $\Pi(s_{\text{in}}, s_{\text{out}})$. White regions mark relative high probabilities. The left panel is computed assuming a uniform distribution of t_E , while the right panel assumes a Gaussian t_E distribution (figures adapted from Cassan et al. 2010).

It is clear however that a uniform distribution on the positions of the entry and exit points on the caustic will not lead to a uniform distribution of α (cf. Fig. 32), as would be expected for random source trajectories. To allow choosing prior distributions on physical parameters such as α , Cassan et al. (2010) derived an analytical expression of the probability density $\Pi(s_{\text{in}}, s_{\text{out}}) = J$ which satisfies $\Pi(\alpha) = 1$, where

$$J = \frac{\left| (\zeta_{\text{out}} - \zeta_{\text{in}}) \wedge \frac{d\zeta_{\text{in}}}{ds_{\text{in}}} \right| \left| (\zeta_{\text{out}} - \zeta_{\text{in}}) \wedge \frac{d\zeta_{\text{out}}}{ds_{\text{out}}} \right|}{|\zeta_{\text{out}} - \zeta_{\text{in}}|^4} \quad (37)$$

is the Jacobian of the transformation $(s_{\text{in}}, s_{\text{out}}, t_{\text{in}}, t_{\text{out}}) \rightarrow (u_0, \alpha, t_E, t_0)$, with $\zeta_1 = \xi_1 + i\eta_1$, $\zeta_2 = \xi_2 + i\eta_2$, $\zeta_1 \wedge \zeta_2 = \xi_1\eta_2 - \eta_1\xi_2$ (“wedge product”) and $\zeta_1 \cdot \zeta_2 = \xi_1\xi_2 + \eta_1\eta_2$ (“scalar product”). The value of J is straightforwardly calculated once the caustics are computed, since the derivatives $d\zeta/ds$ also have analytical expressions (Cassan 2008). More generally, and introducing a Bayesian framework, the prior probability density of the model parameters is expressed as

$$\Pi = \Pi(s_{\text{in}}, s_{\text{out}}) \Pi(t_{\text{in}}, t_{\text{out}}, \beta), \quad (38)$$

where β accounts for other fitting parameters. The probability density of $(s_{\text{in}}, s_{\text{out}})$ then reads $\Pi(s_{\text{in}}, s_{\text{out}}) = J \times \Pi(u_0, \alpha, t_E, t_0)$. Two examples of priors are shown in Fig. 33: the left panel assumes a uniform distribution $\Pi(u_0, \alpha, t_E, t_0) = 1$, while the right panel assumes a Gaussian prior $\Pi(t_E)$ based on the observation of hundreds of microlensing events. From left to right panel, corner regions become black because very small, unphysical values of t_E are very unlikely to occur in a real observation.

This method was applied to the candidate planetary microlensing event OGLE 2007-BLG-472 (Kains et al. 2009), which involved two pronounced caustic crossing anomalies separated by only three days, as shown in Fig. 32. This was a typical example of a very degenerate event, for which a planetary or a binary lens fitted the data. This event provided a critical test which demonstrated the power of the new parametrization to locate all local minima. The resulting ambiguity in the final models discarded the planetary model as the only explanation.

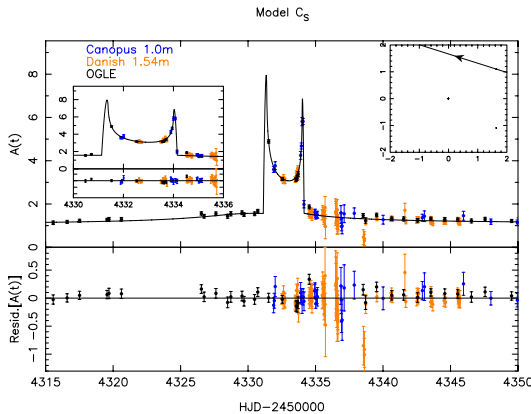


Figure 34: Light curve and one of the best-fit models of microlensing event OGLE 2007-BLG-472. The inset on the left shows the detail of the caustic crossing which is very short. The inset on the right shows the source trajectory (solid line) crossing a tiny secondary, triangular-shape caustic on the upper right (figure from Kains et al. 2009).

3. Bayesian analysis of microlensing events

Kains et al. (2012) developed a fully Bayesian fitting scheme and Markov Chain Monte Carlo algorithm (MCMC) algorithm to analyze efficiently caustic-crossing events based on Cassan (2008)’s parametrization. Appropriate priors include distributions of source radius ρ and timescale t_E derived from Galactic stellar population synthesis models, such as the Besançon model (Robin et al. 2003). The general algorithm is presented in Fig. 35. If the data are called D and the model parameters θ , Bayes’ theorem reads

$$P(\theta|D) = \frac{P(D|\theta) \Pi(\theta)}{\int P(D|\theta) \Pi(\theta) d\theta}, \quad (39)$$

where $\Pi(\theta)$ is the prior and $P(D|\theta)$ is the likelihood (e.g. $P(D|\theta) \propto \exp -\chi^2/2$ for Gaussian errors in the data). The best-fit parameters minimize the “Badness of Fit”, or BoF, with $P(\theta|D) \propto \exp -\text{BoF}/2$. In general, it can lead to notable differences from maximum likelihood (ML) estimates, which maximize $P(D|\theta)$ (*i.e.* minimize χ^2). Different BoF criteria can be used. In a maximum likelihood (ML) analysis, the fit to the data is emphasized, while disregarding priors on the parameters; in a maximum a-posteriori (MAP) analysis, the posterior probability is maximized; the Bayesian Information Criterion (BIC) gives more weight to models that involve fewer fitting parameters; in a fully Bayesian approach, the model that achieves a good fit over a wider range of parameters has a higher probability.

The algorithm was tested on synthetic events and on OGLE 2007-BLG-472 mentioned before. While spurious, unphysical values of t_E as large as a few 10^3 days were found with a classical χ^2 minimization, Bayesian priors led to much more physical solutions ($d = 0.61, q = 0.12$), and definitely discarded the planetary model. Fig. 36 displays the shape of the BoF after a fully Bayesian analysis, for two caustic configurations.

4. Towards automated modeling softwares

In the last decade, the microlensing technique has evolved from a strategy of manual follow-up of selected microlensing targets (1995-2009), to a more automated survey including networks of robotic telescopes with wide-field cameras. A huge flow of data is thus expected, which current modeling softwares cannot handle. This is mainly because many manual operations are still necessary. Hence, it seems critical to develop quickly more automated softwares, which will be the key for future large scale microlensing planet search.

Automated fitting codes should primarily rely on recognizing light curve features and selecting appropriate models with proposed initial parameters. Unless this is achieved, there is very little chance that a model can be automatically found in a reasonable time. The code should also be designed as fully Bayesian, to take advantage of prior information that have been gathered on observed microlensing events or which can be obtained from other sources, such as Galactic models. All available information on the event (light curve parameters, bright-

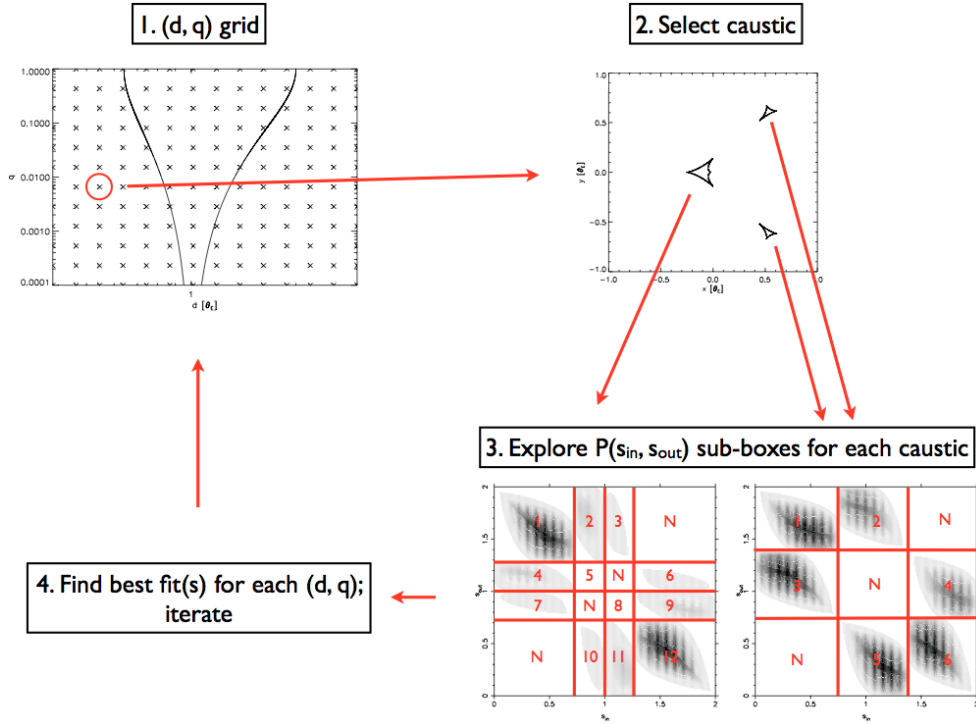


Figure 35: Fitting scheme and algorithm flow of the Bayesian binary-lens algorithm of Kains et al. (2012). Each caustic is treated independently, and for a given caustic, each sub-box (s_{in}, s_{out}) is treated separately before being recombined with the others (figure from Kains et al. 2012).

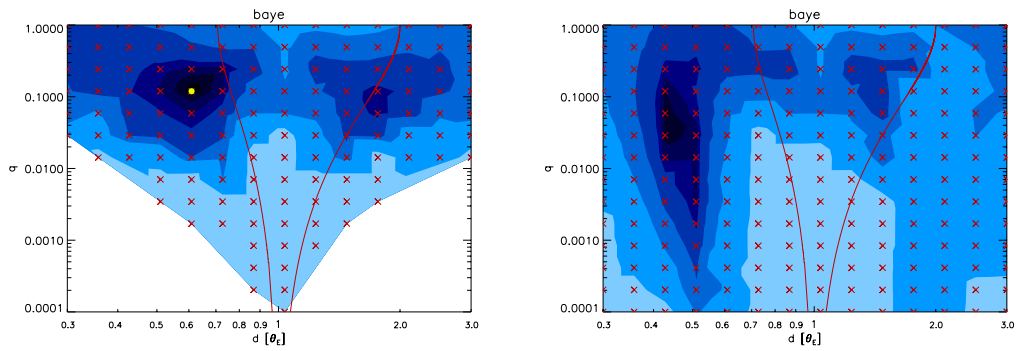


Figure 36: Contour plot of BoF for a fully Bayesian fit of OGLE 2007-BLG-472 data, as a function of binary-lens separation d and mass ratio q . The left panel corresponds to posterior maps $P(d, q|D)$ for the source crossing the central caustic, while the right panel involves a secondary caustic crossing. The filled yellow circle (left) marks the location of the best-fit model (figures adapted from Kains et al. 2012).

ness of the event, duration, high-resolution images...) can then be integrated in a global framework to assess the most likely nature of an event.

As an *online* tool, an automated software should deliver observing recommendations (priorities, observing rate) to robotic telescopes, in order to optimize the detection efficiency. This may ensure that critical short-lived features in the light curve are not missed. As an *offline* tool, it should be an easy-to-use software with a user-friendly graphical interface. It should be fast to get started with it, so that many more events can be analyzed, even by non-specialists. As for many astronomy numerical codes today, the software should be open-source under an appropriate license, and free for download. The recent progresses in modeling are very encouraging signs that this can be achieved in the near future.

V. Summary and prospects

Gravitational microlensing was proposed thirty years ago as a promising method to probe the existence and properties of compact objects in the Galaxy and its surroundings. The particularity and strength of the technique is based on the fact that the detection does not rely on the detection of the photon emission of the object itself, but on the way its mass affects the path of light of a background, almost aligned source. Detections thus include not only bright, but also dark objects. Today, the many successes of gravitational microlensing have largely exceeded the original promises.

Microlensing contributed important results and breakthroughs in several astrophysical fields, in particular: probing the Galactic structure including the measurement of proper motions and extinction maps, searching for dark matter in the form of compact objects in the halo and disk of the Milky Way, probing the atmospheres of bulge red giant stars, searching for low-mass stars and brown dwarfs and hunting for extrasolar planets.

As an extrasolar planet detection method, microlensing nowadays stands in the top five of the successful observational techniques. Compared to other (complementary) detection methods, microlensing provides unique information on the population of exoplanets, because it allows the detection of very low-mass planets (down to the mass of the Earth) at large orbital distances from their star (0.5 to 10 AU). It is also the only technique that allows the discovery of planets at distances from Earth greater than a few kiloparsecs, up to the bulge of the Galaxy.

Microlensing discoveries include the first ever detection of a cool super-Earth ($5 M_{\oplus}$ on a 3-AU orbit) around an M-dwarf star, the detection of several cool Neptunes, Jupiters and super-Jupiters, as well as multi-planetary systems and brown dwarfs. So far, the least massive planet detected by microlensing has only three times the mass of the Earth and orbits a very low mass star at the edge of the brown dwarf regime. Several free-floating planetary-mass objects, including free-floating planets of about Jupiter's mass, were also recently detected through microlensing. Detections and non-detections inform us on the abundance of planets as a function of planetary mass. Recent microlensing studies imply

that low-mass planets, in particular super-Earths, are far more abundant than giant planets, and reveal that there are, on average, one or more bound planets per Milky Way star.

Open questions and challenges

The first planets outside our Solar system were detected only 20 years ago, and extrasolar planetology today is a very active and abounding field of Astronomy. Many questions opened in recent years are still pending, and new issues emerged while hoping to answer them. In this emerging picture, microlensing observations will keep playing a key role in tackling important questions about extrasolar planets. Microlensing has a special sensitivity to planets located far from their stars, and probe a complementary population of planets found by other techniques. The expected increase in planet detections through microlensing will help to better understand the mechanisms at work in planet formation.

Several cases of super-Jupiter planets have been reported around M-dwarf stars from microlensing observations. These planets pose a challenge to the widely accepted mechanism of planet formation, the so-called core accretion model, because building a massive core and subsequently capturing a dense atmosphere is very inefficient around low-mass stars. When more detections are gathered by microlensing and other techniques, it will become possible to compare the frequency of giant and super-giant planets as a function of orbital distance and obtain new observational constraints on planet formation scenarios. In addition, a substantial fraction of the giant planets detected through microlensing are located beyond the ice line, where such planets are supposed to form. More detection will yield the fraction of giant planets located within or beyond the snow line, and provide unprecedented constraints on the speed and efficiency of orbital migration.

Objects with intermediate masses between stars and planets, classically referred to as brown dwarfs, are currently the focus of several questions. It was originally believed that there should exist a mass transition between objects formed by accretion of a solid core in the disc and those formed by gravitational collapse (in the disk or directly in the nebula). Today, the picture has dramatically changed and many pieces of evidence converge toward the idea of an overlap of mechanisms in the range of masses traditionally attributed to brown dwarfs. In the coming years, the advent of robotic telescopes will allow a much more detailed view of the properties of objects populating the mass domain between super-Jupiters and low-mass stars.

Free-floating planetary mass objects provide important information on the final stage of planet formation. While the least massive objects were probably ejected from their parent planetary system because of instabilities such as planet-planet scattering interactions, more massive objects (a few Jupiter masses) may have formed directly via gravitational instability. In the near future, many more free-floating planets will be detected through microlensing, which should provide a much more precise determination of the mass function of free-floating objects.

Microlensing observations are also sensitive to the presence of moons around exoplanets. A serious moon-planet system candidate has already been detected,

but it was not possible to disentangle this scenario from a star-planet system scenario. In the future, microlensing should unambiguously detect moons of giant planets.

Finally, the search for an Earth twin is still an important goal of planet detection, and microlensing observations are getting closer to achieve it.

Prospects on future microlensing surveys

The scientific challenges mentioned here are within the reach of future microlensing searches, thanks to important advances in instrument sensitivity and efficiency of modeling tools.

With 700 alerts per year in 2009 to about 2500 in 2011, the OGLE collaboration has already quadrupled its number of alerted microlensing events. New generations of robotic telescopes equipped with wide-field cameras (KM-NET, LCOGT) are joining the microlensing networks, complementing earlier-generations telescopes (OGLE IV, MOA II, PLANET, μ FUN, RoboNET, MiND-STEp) together with an increasing number of amateur telescopes.

The growing number of light curves requires the implementation of high performance and automated modeling tools working in real time. Bayesian inference is the method of choice in microlensing modeling, and significant progresses were made in the last few years. We should expect important improvements in the future, as statistical methods are being more and more understood and used in astrophysical modeling.

Microlensing observations from space have been proposed onboard the Euclid satellite (ESA, launch in 2020) and WFIRST (NASA, planning phase). Simulations show that for such space-based microlensing missions a great number of planets, including Earth-like planets, should be detected in a few months, and unprecedented constraints on the planetary mass function down to the mass of the Earth should be obtained.

References

- Abe, F., Bennett, D. P., Bond, I. A., et al. 2003, *Astron. Astrophys.*, 411, L493
- Afonso, C., Alard, C., Albert, J. N., et al. 2000, *Astrophys. J.*, 532, 340
- Afonso, C., Albert, J. N., Alard, C., et al. 2003, *Astron. Astrophys.*, 404, 145
- Afonso, C., Albert, J. N., Andersen, J., et al. 2001, *Astron. Astrophys.*, 378, 1014
- Alard, C. 2000, *Astron. Astrophys. Sup.*, 144, 363
- Alard, C. & Guibert, J. 1997, *Astron. Astrophys.*, 326, 1
- Alard, C. & Lupton, R. H. 1998, *Astrophys. J.*, 503, 325
- Albrow, M., Beaulieu, J.-P., Birch, P., et al. 1998, *Astrophys. J.*, 509, 687
- Albrow, M. D. 2004, *Astrophys. J.*, 607, 821

- Albrow, M. D., An, J., Beaulieu, J.-P., et al. 2001, *Astrophys. J.*, 549, 759
- Albrow, M. D., Beaulieu, J.-P., Caldwell, J. A. R., et al. 1999, *Astrophys. J.*, 522, 1022
- Albrow, M. D., Beaulieu, J.-P., Caldwell, J. A. R., et al. 2000, *Astrophys. J.*, 534, 894
- Albrow, M. D., Horne, K., Bramich, D. M., et al. 2009, *Mon. Not. R. Astron. Soc.*, 397, 2099
- Alcock, C., Akerlof, C. W., Allsman, R. A., et al. 1993, *Nature*, 365, 621
- Alcock, C., Allen, W. H., Allsman, R. A., et al. 1997, *Astrophys. J.*, 491, 436
- Alcock, C., Allsman, R. A., Alves, D. R., et al. 2001, *Nature*, 414, 617
- An, J. H. 2005, *Mon. Not. R. Astron. Soc.*, 356, 1409
- An, J. H., Albrow, M. D., Beaulieu, J.-P., et al. 2002, *Astrophys. J.*, 572, 521
- Aubourg, E., Bareyre, P., Bréhin, S., et al. 1993, *Nature*, 365, 623
- Bachelet, E., Fouqué, P., Han, C., et al. 2012, *Astron. Astrophys.*, 547, A55
- Baraffe, I., Chabrier, G., & Barman, T. 2008, *Astron. Astrophys.*, 482, 315
- Batista, V., Dong, S., Gould, A., et al. 2009, *Astron. Astrophys.*, 508, 467
- Batista, V., Gould, A., Dieters, S., et al. 2011, *Astron. Astrophys.*, 529, A102
- Beaulieu, J. P., Bennett, D. P., Batista, V., et al. 2010, *ArXiv/1001.3349*
- Beaulieu, J.-P., Bennett, D. P., Fouqué, P., et al. 2006, *Nature*, 439, 437
- Belokurov, V. A. & Evans, N. W. 2002, *Mon. Not. R. Astron. Soc.*, 331, 649
- Bennett, D. P., Anderson, J., Bond, I. A., Udalski, A., & Gould, A. 2006, *Astrophys. J.*, 647, L171
- Bennett, D. P., Batista, V., Bond, I. A., et al. 2014, *Astrophys. J.*, 785, 155
- Bennett, D. P., Bond, I. A., Udalski, A., et al. 2008, *Astrophys. J.*, 684, 663
- Bennett, D. P. & Rhie, S. H. 1996, *Astrophys. J.*, 472, 660
- Bennett, D. P. & Rhie, S. H. 2002, *Astrophys. J.*, 574, 985
- Bennett, D. P., Rhie, S. H., Becker, A. C., et al. 1999, *Nature*, 402, 57
- Bond, I. A., Udalski, A., Jaroszyński, M., et al. 2004, *Astrophys. J.*, 606, L155
- Bond, I. A. et al. 2001, *Mon. Not. R. Astron. Soc.*, 327, 868
- Boss, A. P. 2006, *Astrophys. J.*, 637, L137
- Bourassa, R. R. & Kantowski, R. 1975, *Astrophys. J.*, 195, 13
- Bozza, V. 2010, *Mon. Not. R. Astron. Soc.*, 408, 2188
- Bozza, V., Dominik, M., Rattenbury, N. J., et al. 2012, *Mon. Not. R. Astron. Soc.*, 424, 902

- Bramich, D. M. 2008, *Mon. Not. R. Astron. Soc.*, 386, L77
- Burgdorf, M. J., Bramich, D. M., Dominik, M., et al. 2007, *Planet. Space Sci.*, 55, 582
- Burrows, A., Hubbard, W. B., Lunine, J. I., & Liebert, J. 2001, *Rev. Mod. Phys.*, 73, 719
- Caballero, J. A., Béjar, V. J. S., Rebolo, R., et al. 2007, *Astron. Astrophys.*, 470, 903
- Cassan, A. 2005, PhD thesis, Institut d'Astrophysique de Paris / Université Pierre et Marie Curie (Paris VI)
- Cassan, A. 2008, *Astron. Astrophys.*, 491, 587
- Cassan, A., Beaulieu, J. P., Brilliant, S., et al. 2004, *Astron. Astrophys.*, 419, L1
- Cassan, A., Beaulieu, J.-P., Fouqué, P., et al. 2006, *Astron. Astrophys.*, 460, 277
- Cassan, A., Horne, K., Kains, N., Tsapras, Y., & Browne, P. 2010, *Astron. Astrophys.*, 515, A52
- Cassan, A., Kubas, D., Beaulieu, J.-P., et al. 2012, *Nature*, 481, 167
- Castro, S., Pogge, R. W., Rich, R. M., DePoy, D. L., & Gould, A. 2001, *Astrophys. J.*, 548, L197
- Chabrier, G., Baraffe, I., Allard, F., & Hauschildt, P. 2000, *Astrophys. J.*, 542, 464
- Choi, J.-Y., Han, C., Udalski, A., et al. 2013, *Astrophys. J.*, 768, 129
- Choi, J.-Y., Shin, I.-G., Park, S.-Y., et al. 2012, *Astrophys. J.*, 751, 41
- Chung, S.-J., Han, C., Park, B.-G., et al. 2005, *Astrophys. J.*, 630, 535
- Claret, A. 2000, *Astron. Astrophys.*, 363, 1081
- Cumming, A., Butler, R. P., Marcy, G. W., et al. 2008, *Publ. Astron. Soc. Pac.*, 120, 531
- Dalal, N. & Lane, B. F. 2003, *Astrophys. J.*, 589, 199
- Delplancke, F., Górski, K. M., & Richichi, A. 2001, *Astron. Astrophys.*, 375, 701
- Dominik, M. 1999, *Astron. Astrophys.*, 349, 108
- Dominik, M. 2007, *Mon. Not. R. Astron. Soc.*, 377, 1679
- Dominik, M., Rattenbury, N. J., Allan, A., et al. 2007, *Mon. Not. R. Astron. Soc.*, 380, 792
- Dong, S., Gould, A., Udalski, A., et al. 2009, *Astrophys. J.*, 695, 970
- Ehrenreich, D. & Cassan, A. 2007, *Astron. Nach.*, 328, 789
- Erdl, H. & Schneider, P. 1993, *Astron. Astrophys.*, 268, 453
- Fields, D. L., Albrow, M. D., An, J., et al. 2003, *Astrophys. J.*, 596, 1305
- Fouqué, P., Heyrovský, D., Dong, S., et al. 2010, *Astron. Astrophys.*, 518, A51

- Gaudi, B. S. 2012, *ARA&A*, 50, 411
- Gaudi, B. S., Bennett, D. P., Udalski, A., et al. 2008, *Science*, 319, 927
- Gaudi, B. S. & Gould, A. 1999, *Astrophys. J.*, 513, 619
- Gaudi, B. S. & Petters, A. O. 2002, *Astrophys. J.*, 574, 970
- Gaudi, B. S. & Sackett, P. D. 2000, *Astrophys. J.*, 528, 56
- Gaudi, B. S. et al. 2002, *Astrophys. J.*, 566, 463
- Ghosh, H., DePoy, D. L., Gal-Yam, A., et al. 2004, *Astrophys. J.*, 615, 450
- Gould, A. 1994, *Astrophys. J.*, 421, L71
- Gould, A. 2004, *Astrophys. J.*, 606, 319
- Gould, A. 2008, *Astrophys. J.*, 681, 1593
- Gould, A. 2009, in *Astronomy*, Vol. 2010, *astro2010: The Astronomy and Astrophysics Decadal Survey*, 100
- Gould, A., Dong, S., Bennett, D. P., et al. 2010a, *Astrophys. J.*, 710, 1800
- Gould, A., Dong, S., Gaudi, B. S., et al. 2010b, *Astrophys. J.*, 720, 1073
- Gould, A. & Gauchere, C. 1997, *Astrophys. J.*, 477, 580
- Gould, A. & Horne, K. 2013, *ArXiv e-prints*
- Gould, A. & Loeb, A. 1992, *Astrophys. J.*, 396, 104
- Gould, A., Udalski, A., An, D., et al. 2006, *Astrophys. J.*, 644, L37
- Gould, A., Udalski, A., Monard, B., et al. 2009, *Astrophys. J.*, 698, L147
- Gould, A. & Yee, J. C. 2013, *Astrophys. J.*, 764, 107
- Gould, A., Yee, J. C., Bond, I. A., et al. 2013, *Astrophys. J.*, 763, 141
- Griest, K. & Safizadeh, N. 1998, *Astrophys. J.*, 500, 37
- Guillot, T., Lin, D. N. C., & Morel, P. 2012, *AA Meeting Abstracts*, 220, 121
- Gustafsson, B., Edvardsson, B., Eriksson, K., et al. 2008, *Astron. Astrophys.*, 486, 951
- Han, C. 2006, *Astrophys. J.*, 638, 1080
- Han, C. & Gould, A. 1995, *Astrophys. J.*, 449, 521
- Han, C., Jung, Y. K., Udalski, A., et al. 2013, *Astrophys. J.*, 778, 38
- Hardy, S. J. & Walker, M. A. 1995, *Mon. Not. R. Astron. Soc.*, 276, L79
- Hendry, M. A., Coleman, I. J., Gray, N., Newsam, A. M., & Simmons, J. F. L. 1998, *New Astron. Rev.*, 42, 125
- Hennebelle, P. & Chabrier, G. 2008, *Astrophys. J.*, 684, 395
- Heyrovský, D. 2007, *Astrophys. J.*, 656, 483

- Heyrovský, D., Sasselov, D., & Loeb, A. 2000, *Astrophys. J.*, 543, 406
- Holz, D. E. & Wald, R. M. 1996, *Astrophys. J.*, 471, 64
- Horne, K., Snodgrass, C., & Tsapras, Y. 2009, *Mon. Not. R. Astron. Soc.*, 396, 2087
- Hwang, K.-H., Udalski, A., Han, C., et al. 2010, *Astrophys. J.*, 723, 797
- Ida, S. & Lin, D. N. C. 2005, *Astrophys. J.*, 626, 1045
- Jaroszynski, M. 2002, *Acta Astron.*, 52, 39
- Jaroszynski, M., Skowron, J., Udalski, A., et al. 2006, *Acta Astron.*, 56, 307
- Jaroszynski, M., Udalski, A., Kubiak, M., et al. 2004, *Acta Astron.*, 54, 103
- Jaroszynski, M., Udalski, A., Kubiak, M., et al. 2005, *Acta Astron.*, 55, 159
- Jiang, G., DePoy, D. L., Gal-Yam, A., et al. 2004, *Astrophys. J.*, 617, 1307
- Jung, Y. K., Han, C., Gould, A., & Maoz, D. 2013, *Astrophys. J.*, 768, L7
- Kains, N., Browne, P., Horne, K., Hundertmark, M., & Cassan, A. 2012, *Mon. Not. R. Astron. Soc.*, 426, 2228
- Kains, N., Cassan, A., Horne, K., et al. 2009, *Mon. Not. R. Astron. Soc.*, 395, 787
- Kains, N., Street, R. A., Choi, J.-Y., et al. 2013, *Astron. Astrophys.*, 552, A70
- Kennedy, G. M. & Kenyon, S. J. 2008, *Astrophys. J.*, 673, 502
- Kerins, E., Robin, A. C., & Marshall, D. J. 2009, *Mon. Not. R. Astron. Soc.*, 396, 1202
- Kervella, P. & Fouqué, P. 2008, *Astron. Astrophys.*, 491, 855
- Kiraga, M. & Paczynski, B. 1994, *Astrophys. J.*, 430, L101
- Kubas, D. 2005, PhD thesis, Applications of Galactic Microlensing, University of Potsdam
- Kubas, D., Beaulieu, J. P., Bennett, D. P., et al. 2012, *Astron. Astrophys.*, 540, A78
- Kubas, D., Cassan, A., Beaulieu, J. P., et al. 2005, *Astron. Astrophys.*, 435, 941
- Kubas, D., Cassan, A., Dominik, M., et al. 2008, *Astron. Astrophys.*, 483, 317
- Kurucz, R. L. 1992, in *IAU Symposium*, Vol. 149, The Stellar Populations of Galaxies, ed. B. Barbuy & A. Renzini, 225
- Laughlin, G., Bodenheimer, P., & Adams, F. C. 2004, *Astrophys. J.*, 612, L73
- Leconte, J., Chabrier, G., Baraffe, I., & Levrard, B. 2010, *Astron. Astrophys.*, 516, A64
- Liebig, C. & Wambsganss, J. 2010, *Astron. Astrophys.*, 520, A68
- Liu, M. C., Magnier, E. A., Deacon, N. R., et al. 2013, *ArXiv e-prints*
- Loeb, A. & Sasselov, D. 1995, *Astrophys. J.*, 449, L33
- Luhman, K. L., Adame, L., D'Alessio, P., et al. 2005, *Astrophys. J.*, 635, L93

- Ma, B. & Ge, J. 2014, *Mon. Not. R. Astron. Soc.*, 439, 2781
- Mao, S. 2012, *Research in Astronomy and Astrophysics*, 12, 947
- Mao, S. & Paczynski, B. 1991, *Astrophys. J.*, 374, L37
- Marboeuf, U., Mousis, O., Ehrenreich, D., et al. 2008, *Astrophys. J.*, 681, 1624
- Marcy, G. W. & Butler, R. P. 2000, *Publ. Astron. Soc. Pac.*, 112, 137
- Mayor, M. & Queloz, D. 1995, *Nature*, 378, 355
- Miyake, N., Udalski, A., Sumi, T., et al. 2012, *Astrophys. J.*, 752, 82
- Mordasini, C., Alibert, Y., Benz, W., & Naef, D. 2009, *Astron. Astrophys.*, 501, 1161
- Muraki, Y., Han, C., Bennett, D. P., et al. 2011, *Astrophys. J.*, 741, 22
- Nakajima, T., Oppenheimer, B. R., Kulkarni, S. R., et al. 1995, *Nature*, 378, 463
- Oppenheimer, B. R., Kulkarni, S. R., Matthews, K., & Nakajima, T. 1995, *Science*, 270, 1478
- Paczynski, B. 1986, *Astrophys. J.*, 304, 1
- Paczynski, B. 1996, *ARA&A*, 34, 419
- Paczynski, B. & Stanek, K. Z. 1998, *Astrophys. J.*, 494, L219
- Pejcha, O. & Heyrovský, D. 2009, *Astrophys. J.*, 690, 1772
- Penny, M. T., Kerins, E., Rattenbury, N., et al. 2013, *Mon. Not. R. Astron. Soc.*, 434, 2
- Penny, M. T., Mao, S., & Kerins, E. 2011, *Mon. Not. R. Astron. Soc.*, 412, 607
- Perryman, M. 2012, *Astrobiology*, 12, 928
- Petters, A. O., Levine, H., & Wambsganss, J. 2001, *Birkhäuser*, 21
- Plez, B., Brett, J. M., & Nordlund, A. 1992, *Astron. Astrophys.*, 256, 551
- Poleski, R., Udalski, A., Dong, S., et al. 2014, *Astrophys. J.*, 782, 47
- Poteet, W. M., Cauten, H. K., Kappler, N., et al. 2012, *SPIE*, 8444, 5
- Quanz, S. P., Goldman, B., Henning, T., et al. 2010, *Astrophys. J.*, 708, 770
- Rattenbury, N. J. & Mao, S. 2006, *Mon. Not. R. Astron. Soc.*, 365, 792
- Rebolo, R., Zapatero Osorio, M. R., & Martín, E. L. 1995, *Nature*, 377, 129
- Rhie, S. H. 2003, *ArXiv Astrophysics e-prints*
- Rhie, S. H., Bennett, D. P., Becker, A. C., et al. 2000, *Astrophys. J.*, 533, 378
- Robin, A. C., Reylé, C., Derrière, S., & Picaud, S. 2003, *Astron. Astrophys.*, 409, 523
- Sahlmann, J., Ségransan, D., Queloz, D., et al. 2011, *Astron. Astrophys.*, 525, A95
- Sahu, K. C., Casertano, S., Livio, M., et al. 2001, *Nature*, 411, 1022

- Sasselov, D. D. 1996, ASPSC, 109, 541
- Schechter, P. L., Mateo, M., & Saha, A. 1993, Publ. Astron. Soc. Pac., 105, 1342
- Schneider, P. & Weiss, A. 1986, Astron. Astrophys., 164, 237
- Shin, I.-G., Choi, J.-Y., Park, S.-Y., et al. 2012a, Astrophys. J., 746, 127
- Shin, I.-G., Han, C., Choi, J.-Y., et al. 2012b, Astrophys. J., 755, 91
- Shin, I.-G., Han, C., Gould, A., et al. 2012c, Astrophys. J., 760, 116
- Shin, I.-G., Udalski, A., Han, C., et al. 2011, Astrophys. J., 735, 85
- Skowron, J., Jaroszynski, M., Udalski, A., et al. 2007, Acta Astron., 57, 281
- Smith, M. C., Belokurov, V., Evans, N. W., Mao, S., & An, J. H. 2005, Mon. Not. R. Astron. Soc., 361, 128
- Smith, M. C., Mao, S., & Paczyński, B. 2003, Mon. Not. R. Astron. Soc., 339, 925
- Snodgrass, C. et al. 2004, Mon. Not. R. Astron. Soc., 351, 967
- Street, R. A., Choi, J.-Y., Tsapras, Y., et al. 2013, Astrophys. J., 763, 67
- Sumi, T., Bennett, D. P., Bond, I. A., et al. 2010, Astrophys. J., 710, 1641
- Sumi, T., Kamiya, K., Bennett, D. P., et al. 2011, Nature, 473, 349
- Sumi, T., Woźniak, P. R., Udalski, A., et al. 2006, Astrophys. J., 636, 240
- Tisserand, P., Le Guillou, L., Afonso, C., et al. 2007, Astron. Astrophys., 469, 387
- Tsapras, Y., Street, R., Horne, K., et al. 2009, Astron. Nach., 330, 4
- Tsapras, Y. et al. 2003, Mon. Not. R. Astron. Soc., 343, 1131
- Udalski, A. 2003, Acta Astron., 53, 291
- Udalski, A., Szymanski, M., Mao, S., et al. 1994, Astrophys. J., 436, L103
- Udalski, A. et al. 2005, Astrophys. J., 628, L109
- Wambsganss, J. 1997, Mon. Not. R. Astron. Soc., 284, 172
- Witt, H. J. 1990, Astron. Astrophys., 236, 311
- Witt, H. J. 1995, Astrophys. J., 449, 42
- Witt, H. J. & Mao, S. 1994, Astrophys. J., 430, 505
- Witt, H. J. & Mao, S. 1995, Astrophys. J., 447, L105
- Wolszczan, A. & Frail, D. A. 1992, Nature, 355, 145
- Wyrzykowski, L., Skowron, J., Kozłowski, S., et al. 2011, Mon. Not. R. Astron. Soc., 416, 2949
- Yock, P., Bond, I., Rattenbury, N., et al. 2000, ArXiv astro-ph/0007317
- Yoo, J., DePoy, D. L., Gal-Yam, A., et al. 2004, Astrophys. J., 603, 139

Zakharov, A. F. 1995, *Astron. Astrophys.*, 293, 1

Zapatero Osorio, M. R., Béjar, V. J. S., Martín, E. L., et al. 2000, *Science*, 290, 103

Zub, M., Cassan, A., Heyrovský, D., et al. 2011, *Astron. Astrophys.*, 525, A15